Femtosecond Laser Fabrication and Optical Characterization of Low-Loss Diamond Waveguides

by

Faik Derya INCE

A Dissertation Submitted to the
Graduate School of Sciences and Engineering
in Partial Fulfillment of the Requirements for
the Degree of

Master of Science

in

Material Science and Engineering

KOÇ
ÜNİVERSİTESİ

July, 2023

Femtosecond Laser Fabrication and Optical Characterization of Low-Loss Diamond Waveguides

Koç University

Graduate School of Sciences and Engineering

This is to certify that I have examined this copy of a master's thesis by

Faik Derya INCE

and have found that it is complete and satisfactory in all respects,
and that any and all revisions required by the final
examining committee have been made.

Committee Members:

_____

Prof. Dr. Alphan Sennaroglu (Advisor)

_____

Assist. Prof. Onur Ferhanoglu

_____

Research Assist. Prof. Yagiz Morova

Date: _____

To Ufuk Diker, who may rest in peace…

ABSTRACT

Femtosecond Laser Fabrication and Optical Characterization of Low-Loss Diamond Waveguides

Master of Science in Material Science and Engineering

July 27, 2023

In addition to its excellent mechanical and thermal properties, diamond also possesses favorable linear and nonlinear optical properties, including a wide spectral transparency window from the ultraviolet to infrared, a high refractive index, and a reasonably high nonlinear refractive index, among others.

In recent years, diamond has also been demonstrated as a promising platform for quantum information and sensing applications due to the presence of spin-active nitrogen vacancy centers (NV) with long coherence times at room temperature. These NV centers generate spin-dependent fluorescence when excited at 532 nm and enable the measurement of numerous physical quantities such as strain, magnetic field, and temperature with high sensitivity. In such quantum sensing applications, optical waveguides play a crucial role, since they can be used for addressing and spatially linking NV centers or for guiding fluorescence between different locations inside the diamond crystal.

In this thesis, fabrication and optical characterization of femtosecond (fs) laser written waveguides with varying geometries and parameters in a single crystal CVD grown diamond has been demonstrated. Depressed circular cladding, half-ring, and double-line waveguides were fabricated. Design parameters such as core size and number of written tracks were varied to minimize propagation losses. Characterization of the waveguides was performed at 633 nm, which is close to the peak fluorescence wavelength of the nitrogen NV centers in diamond. Important experimental results revealing the dependence of the propagation loss and refractive index contrast on the design parameters were obtained. The maximum refractive index contrast was estimated as 22.7×10^{-5} for the fabricated waveguides. The measured propagation loss values of 2.05 dB/cm and 1.20 dB/cm, obtained with circular depressed cladding and half-ring waveguides, respectively, are, to the best of our knowledge, the lowest propagation loss values reported so far among fs laser written diamond waveguides. It is forseen that the photonic devices based

on the diamond waveguides examined in this thesis can find applications in quantum communication.

ÖZETÇE

Düşük Kayıplı Elmas Dalga Kılavuzlarının Femtosaniye Lazer ile Üretimi ve Optik Karakterizasyonu

Malzeme Bilimi ve Mühendisliği, Yüksek Lisans

27 Temmuz 2023

Elmas, sıradışı mekanik ve termal özelliklerinin yanısıra, morötesinden kızılötesine kadar geniş bir spektral transparan aralık, yüksek kırılma indisi, ve görece yüksek bir lineer olmayan kırılma indisi gibi birçok faydalı optik özellik barındırmaktadır.

Son yıllarda, elmas, yapısında bulundurduğu, oda sıcaklığında yüksek eşevrelilik sürelerine sahip spin-aktif azot-boşluk (NV) merkezleri sayesinde gelecek vaadeden bir kuantum haberleşme platformu olarak gösterilmiştir. Bu NV merkezleri, 532 nm dalga boyunda uyarıldığında spine bağlı ışıma gerçekleştirerek manyetik alan, sıcaklık ve gerilim gibi birçok fiziksel niceliğin oldukça hassas ölçümünü sağlamaktadır. Bu tür quantum ölçüm uygulamalarında, optik dalga kılavuzları; hem birçok NV merkezinin uzamsal olarak bağlanmasını hem de NV merkezlerinin yaydığı ışıma sinyalinin elmas kristali içerisindeki farklı noktalara iletilmesini sağladığı için oldukça önemli rol oynamaktadır.

Bu tezde, farklı geometrik konfigürasyonlara ve üretim parametrelerine sahip çeşitli optik dalga kılavuzları, kimyasal buhar yığma (CVD) yöntemi ile büyütülmüş tek kristal elmas içerisine yazılmıştır. Yüzey altına gömülü dairesel kılıflı, yarım dairesel ve çift çizgili olmak üzere üç tür dalga kılavuzu üretilmiştir. Kılavuzlayan çekirdek boyutu ve çizgi sayısı gibi tasarım parametreleri, üretilen dalga kılavuzlarının yayılma kayıplarını azaltmak için geniş bir aralıkta değiştirilmiş ve en uygun değerler deneysel olarak saptanmıştır. Dalga kılavuzlarının optik karakterizasyonu, NV merkezlerinin tepe ışıma dalga boyuna yakın olan 633 nm dalga boyunda He-Ne lazeri kullanılarak gerçekleştirilmiştir. Yayılma kaybının ve kırılma indisi kontrastının tasarım parametrelerine olan bağımlılığını gösteren önemli deneysel sonuçlar elde edilmiştir. Üretilen dalga kılavuzlarında elde edilen en yüksek kırılma indisi kontrastı 22.7×10^{-5} seviyesinde ölçülmüştür. En düşük kayıplı yüzey altına gömülü dairesel kılıflı ve yarım

dairesel dalga kılavuzlarından elde edilen, sırasıyla, 2.05 ve 1.20 dB/cm miktarındaki yayılma kaybı değerleri, bilindiği kadarıyla, şu ana kadar literatürde raporlanan fs lazer ile yazılan elmas dalga kılavuzları arasındaki en düşük kayıp miktarlarıdır. Bu tezde incelenen elmas dalga kılavuzu tabanlı fotonik aygıtların yeni nesil kuantum haberleşme sistemlerinde uygulamalar bulabileceği ön görülmektedir.

AKNOWLEDGEMENTS

It is impossible to thank enough to my thesis advisor Prof. Dr. Alphan Sennaroğlu. I was just a mechanical engineer and I had literally no clue what a laser, photon, or even wavelength was. However, he saw my motivation and willingness to learn new things and he patiently trained me in the field of photonics *like a master who trains his apprentice* from ground zero. When I look back, I see that the radical change that I did from mechanical engineering to photonics and material science was the best choice of my life so far, all of which thanks to the Professor Sennaroğlu.

Dr. Yağız Morova took a crucial role during my masters, he carved me as if I'm a piece of wood in our laboratory and turned me into what I am now. Above all, he always approached me in a friendly manner, almost like an *elderly brother* rather than a postdoctoral researcher, and I'm so grateful for this.

I was so lucky to get both financial and technical support from Appsilon Enterprise. They are the sole example of a company that I would like to work if any day in future I would choose to go back to the industry. From Appsilon Enterprise, I especially would like to thank Chief Technology Officer Taylan Erol; the most versatile and *reachable* CTO of history and Umut Yazlar; a friendly *teammate* that every team needs.

I would like to express my gratitudes to Asst. Prof. Dr. Seyed Ehsan Layegh, since he is the one who ignited all this by presenting this MS program and being a reference to me. Without him, I wouldn't be able to switch back to academia and I would be *stuck in the industry as an unhappy and unfulfilled person.*

I also would like to express my sincere thanks to Assoc. Prof. Dr. Onur Ferhanoğlu for his kind interest and time to become a jury member for my thesis committee.

Besides their selfless love and support, my family have always stood behind me; they never made me doubt *even for a second* for any of my choices during my life, which is what I am grateful the most above all.

I would especially like to thank my dearest friend Kubilay Düzgit for all his *consultancy* throughout my masters education. I believe he will become a great consultant in his career as well.

It is impossible to end this acknowledgement without acknowledging my dear labmates. Eylül Nihan Kamun; above all the lab-work you helped, I'm thankful for all the *memories*. I feel so lucky to have your lovely *companionship* and my sincere goal will be

to make this *bond forever*. Emir Ardalı is the one friend every prospective academic would need, I will miss all our *heart-to-heart* talks on academia that lasted for hours. I thank Emir for all his reasonable thoughts and advices and from my heart I believe that he will be rewarded much more than all the *hardwork* he put. I benefitted so much from the physics background of Berke Ayevi and I'm indebted for that. However I thank Berke the most for all the *comedy* and friendful memories that he brought to our laboratory. I also would like to thank Minahil Khan for all her help during my adaptation to the university at my first times, we all miss you so much.

Last but not least, Yunus Gürpınar is the best housemate on the planet. I thank him so much and I believe he will overcome all of his struggles as a wiser person.

TABLE OF CONTENTS

LIST OF TABLES

LIST OF FIGURES

ABBREVIATIONS

CVD	Chemical Vapor Deposition
D	Core Size
HPHT	High Pressure High Temperature
N	Number of Written Tracks
NA	Numerical Aperture
NV	Nitrogen Vacancy
L	Line Height
L1	Lens 1
L2	Lens 2
TE	Transverse Electric
TM	Transverse Magnetic

Chapter 1:
INTRODUCTION

1.1 Laser Material Processing

Shortly after the first demonstration of lasing in ruby by Maiman [1], lasers have been utilized as intense light sources to process and shape materials, firstly demonstrated by Giuliano on dielectric transparent materials [2]. Since then, lasers are considered as effective and efficient tools to alter material properties due to their capability of producing high-intensity light pulses with short duration. In addition, over the last decades, technological advances enabled the production of robust high-intensity lasers which are commercially available [3]. Coherent and confined nature of the light produced by lasers, combined with precise sample positioning or laser beam movement opened up a possibility to fabricate complex three-dimensional structures by machining with lasers on micro-scale; both on the surface as well as inside the bulk of the target material. In addition, the applicability of lasers to modify various materials such as metals [4], semiconductors [5], and dielectrics [6] make lasers well-rounded tools to enhance material properties by laser material processing. Moreover, the process itself is deterministic and versatile since the process parameters such as laser power, scan speed and numerical aperture can be differed on a wide range.

One type of lasers which is advantageous on laser material processing is pulsed lasers, especially femtosecond (fs) lasers, which have laser pulse durations on the order of femtoseconds (10^{-15} seconds). Compressing the laser energy to such a short amount of time inevitably involves nonlinear effects, opens up further possibilities to micromachine any material regardless of the optical properties of the sample. In addition, light-matter interactions on a fs time scale enables one to observe exotic intra-atomic mechanisms. Considering all those, fs laser material processing, or so-called fs laser micromachining has become an emerging tool for fabricating complex and precise structures. Just after ten years of the first demonstration of fs laser micromachining in silica [7], the sensitivity of the process has been reduced down to nanometer scale [8], proving the importance of the technique by such advances over a decade.

1.1.1 Femtosecond Laser Micromachining of Transparent Dielectrics

The mechanism behind fs laser micromachining is optical breakdown. During the laser irradiation, the optical energy of the laser pulse is deposited and transferred to the atomic lattice of the material by ionizing many electrons. Optical breakdown involves nonlinear absorption of the incident laser beam, where the absorption coefficient of the material, therefore the absorption of the incident beam, increases exponentially with the intensity of the incident beam. This nonlinear nature of the optical breakdown is especially advantageous while processing transparent dielectric bulk materials using fs lasers. To process the bulk of a transparent dielectric, the sample material must be non-absorptive at the laser wavelength to be able to reach a certain depth in the bulk of the sample. On the other hand, incident laser beam must be absorbed at the local processing volume inside the material. Both of those competing factors are eliminated by the nonlinear nature of optical breakdown; an incident fs laser beam with a non-resonant wavelength can be focused inside the bulk of a transparent dielectric material without being absorbed, and due to the nonlinear absorption, the incident beam at the focal point can be absorbed by the material. As a result, bulk of the transparent dielectric can be processed. To achieve such nonlinear absorption and optical breakdown, incident laser pulses need to have electric field intensities sufficiently large to overcome the binding energy of the valence band electrons of the material, approximately on the order of 10^7 Vcm^{-1}, which translates to 5×10^{16} Wcm^{-2} [9]. Such electric field magnitudes are available from tightly focused fs laser beams.

During irradiation of fs laser pulses, for pulses having durations greater than 10 fs, the electrons excited by nonlinear absorption and got free by nonlinear ionization can be excited to further energy levels by linear absorption stimulated by phonons. When the electrons reach to a certain kinetic energy, the process called avalanche ionization takes place where a chain reaction of ionization starts by excitation of bound electrons by the nonlinearly excited electrons, leading to a rapid production of ions and free electrons. After the excited electrons' density reaches to a certain threshold, they act as a plasma with a resonant frequency equlas to the frequency of the incident laser beam, resulting as the absorption of the remaining laser pulse energy. This whole process is the main mechanism behind the energy transfer between the electrons and the incident laser pulses [10]. The figure below shows a representative schematic of sequential multiphoton

ionization (a nonlinear ionization process), impact ionization and avalanche ionization processes.

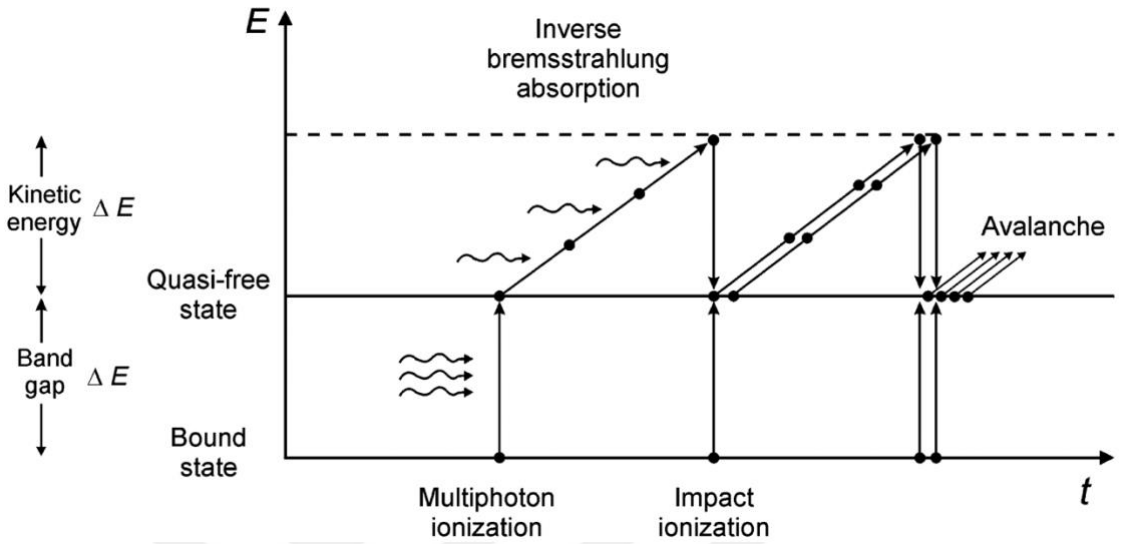

Figure 1.1: A schematic showing the process of multiphoton ionization and avalanche ionization involved in plasma formation during fs laser irradiation (the figure is taken from Ref. [11]).

Figure 1.2. below shows various important timescales of both intra- and inter-atomic events involving interactions between fs laser pulses and the sample material [6]. Between several microseconds, thermal energy inside the lattice diffuses out through the focal volume. On the nanosecond timescale, a shock wave resulting from the energy transfer between the electrons and the lattice is created and propagates throughout the hot and dense focal volume. Within a couple of picoseconds, the absorbed optical energy of the electrons is transferred to the lattice system.

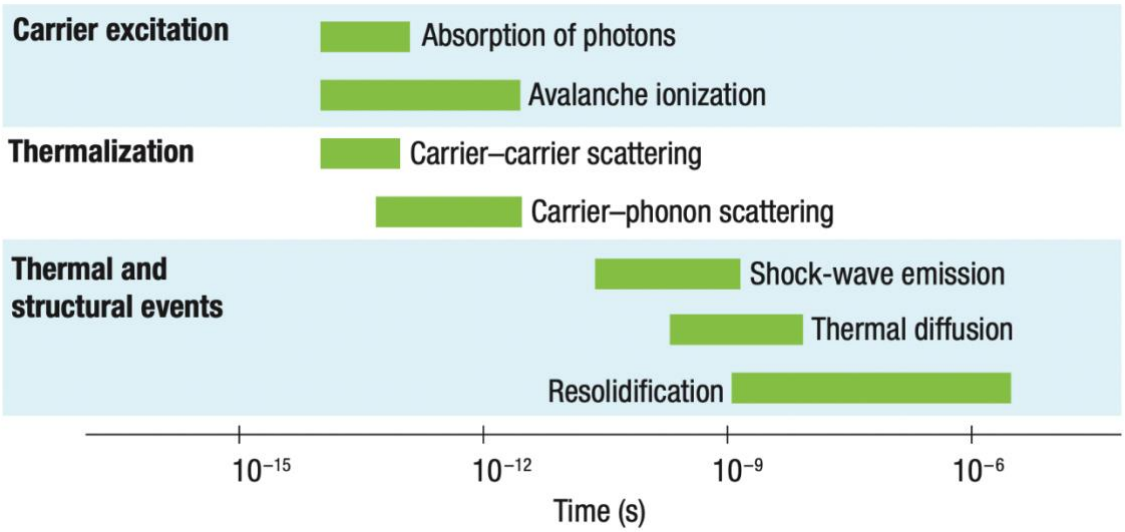

Figure 1.2: Timescale of intra- (carrier excitation and thermalization events) and inter-atomic (thermal and structural events) events after the interaction of a transparent material with fs laser pulses (the figure is taken from Ref. [6]).

Figure 1.2 explains the advantage of the fs lasers on the micromachining applications. As it can be seen, the duration of the fs laser pulse is shorter than the amount of time needed to thermal energy transfer between the electron and the lattice systems. Thus, the heat diffusion from the optical energy transfer is minimized and therefore the material processing volume is confined approximately only to the focal volume of the incident laser pulse, increasing the precision of the process. Apart from this, the nonlinear energy transfer between the fs laser pulse and the electrons mentioned previously (nonlinear ionization) eliminates the need of any seed electrons generated previously from the laser pulse-material interaction. Seed electrons needed to start the whole process are already generated within first few femtoseconds of the fs laser pulse by nonlinear ionization [10]. This spatial confinement and deterministic repeatability of fs laser micromachining makes itself an attractive method for high precision material processing. In the figure below, a representative schematic can be seen for an example fs laser micromachining setup.

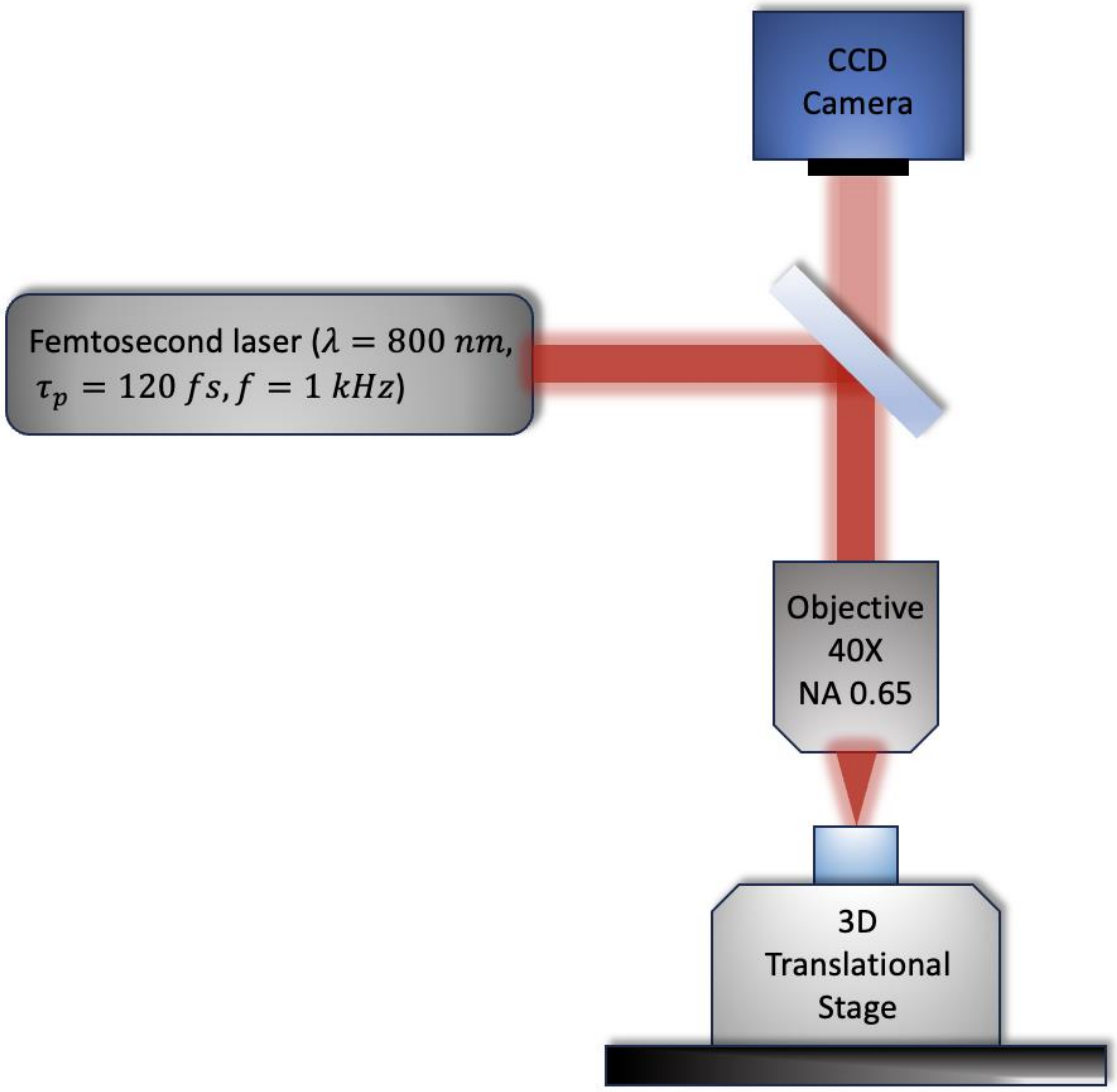

Figure 1.3: A schematic of a fs laser micromachining setup including a CCD camera for process monitoring (fs laser parameters are the same with the laser setup used during the waveguide fabrication in this thesis).

As previously mentioned, the one major advantage of fs laser micromachining, apart from spatial confinement and deterministic repeatability, is the fact that it is a process independent from the processing material thanks to the avalanche ionization. If the energy transfer between electrons and incident laser pulse would be dependent only to nonlinear ionization, then the laser pulse intensity needed to ablate the material would be dependent to the band gap nonlinearly. However, the involvement of avalanche ionization to the process, which is a linear process as mentioned previously, suppresses the nonlinearity coming from nonlinear ionization and makes the process much lesser dependent to the

band gap, leading to the availability of fs laser micromachining to various different materials.

Damage threshold intensity, the minimum laser intensity needed to damage the material, is dependent on three experimental parameters: pulse duration (τ), pulse energy (E), and numerical aperture (NA). The laser intensity depending on those three experimental parameters as well as the given wavelength of the laser (λ) can be found as in the below equation [12]:

$$I \approx \frac{E\ NA^2}{\tau\ \lambda^2(1 - NA^2)} \tag{1.1}$$

Using the equation above, one can estimate the damage threshold intensity of a sample material. As it can be seen from the Eq. (1.1), there is a directly inverse relation between the laser intensity and the τ parameter. On the other hand, experimental results presented to the literature [7, 13] do not follow this directly inverse relation. For τ values longer than 10 ps, threshold intensity follows a $\tau^{0.5}$ relation, meaning that on that pulse duration regime, thermalization due to carrier-phonon scattering dominates for the material damage. When the τ further reduced below 10 ps, for every ten units of decrease on τ, threshold intensity reduces three units, which is because of the avalanche ionization: nonlinear absorption and therefore, nonlinear ionization populates the seed electrons, however; avalanche ionization, which is linearly dependent to the laser intensity, creates the high plasma density needed to damage the material [10]. The small dependency of threshold intensity on τ creates a versitility on the initial selection of any commercial laser, a critical advantage for fs laser micromachining implementations to the industry.

The fs laser micromachining process is strongly dependent on the process parameter *E*, especially when the τ and *NA* kept constant. The minimum E that would populates the inital seed level of the electrons by starting the nonlinear ionization is called threshold energy. When the selected E value is around the threshold value, irradiation of the sample results as a change in the refracive index on the focal volume. The occured index contrast can be both positive and negative, depending on the material. It should be noted that this index contrast is not spatially homogenous and the mechanisms behind it under investigation, such as laser-induced lattice stress and color center formation [14]. Most photonic applications use E values close to the threshold energy value, resulting in index contrasts [6]. Increasing E further from the threshold value both increases the average plasma energy as well as the affected volume of the material from the irradiation. As the

plasma energy increases, shielding effect between the electrons reduces, resulting increased Coloumb repulsion. Sufficent amount of Coloumb repulsion would result as void formation on the focal volume, which is also called ablation [15].

A change in the next process parameter, NA, would determine the volume that occupied at the focal spot by the laser and therefore, the size of the fabricated structure. For the commercially available E values on the order of milijoules, the minimum theoretical NA needed to achieve threshold intensity is around 0.002. However, in real life, the minimum NA value needs to be higher than that value because of two nonlinear processes competing with energy deposition with laser irradiation: First one is self-focusing, the undesired change in the shape of the propagating wavefront which results as collapse of the pulse into a filament with a smaller diameter [16]; the second one is white light generation, which causes a broadening on the spectrum of the pulse [17]. Both of those nonlinear processes are intensity dependent. When NA<0.1, the threshold intensity of those two nonlinearities are below the damage threshold intensity. Therefore, the experimental minimum of the NA is 0.1 [12].

1.1.2 Femtosecond Laser Written Dielectric Waveguides

In the field of integrated photonics, optical waveguides are small devices used to confine and manipulate the propagation of any input electromagnetic wave inside their structure. The primary aim of a waveguide is to confine light in a spatial location and enable its transfer between selected locations in a solid with minimum optical loss. Waveguides achieve this by confining the input electromagnetic modes within the spatial extend of the waveguide. Mainly, depending on the material used to build the waveguide, there are two types of waveguides: metal waveguides and dielectric waveguides. In the context of this section, dielectric waveguides will be the main focus. The confinement inside the dielectric waveguide structure is reached by the refractive index contrast. Typically, inside a waveguide structure, there are two distinct regions: a high refractive index core and the surrounding lower refractive index cladding. The refractive index contrast occurred between the core and the cladding region would result as the phenomenon called total internal reflection, where an electromagnetic wave with a given wavelength reflects from the core-cladding interface with an acceptance angle depending on the amount of refractive index contrast achieved. In general, waveguides have very

small volumes, which make them quite compact and useful devices for signal processing applications and development of integrated photonic devices [18]. Moreover, waveguides are highly efficient in terms of achieving very high light intensities thanks to their confinement inside their small volume, which results as enhancement of certain photonic processes compared to their bulk operations, such as improving laser features by waveguide lasers and nonlinear optics applications [19, 20]. In addition to those, waveguides can be used as wavelength filters, mode filters, mode splitters and mode combiners [21].

Fabrication of waveguides with diverse configurations and geometries is an important task to fulfill for addressing different photonic applications. Those fabrication techniques are including metal-ion diffusion [22], chemical vapor deposition and epitaxial layer deposition [23], ion/proton exchange [24], ion-beam implantation, pulsed laser deposition [25] and fs laser micromachining [26].

As mentioned before, the nonlinear ionization and avalanche ionization involved during fs laser micromachining offers local change in the refractive index confined only to the focal volume of the irradiated material, since the thermal diffusion is eliminated. This provides a possibility to fabricate structures with a refractive index contrast (Δn) on a sub-micron scale. Combination of those features with 3D sample translation or beam scanning makes fs laser micromachining a suitable technique for fabrication of optical waveguides inside transparent dielectric materials. Depending on the material properties as well as to the process parameters, both positive ($\Delta n>0$) and negative ($\Delta n<0$) changes on the local refractive index of the material can be created [26]. In addition, this technique doesn't demand any clean room environment or special sample preparation, making it direct and versatile for waveguide fabrication. Moreover, thanks to the nonlinear absorption during fs laser irradiation, waveguide fabrication using fs laser micromachining has been realized on wide range of materials from amorphous glasses to single crystal dielectrics [27]. All those factors considered, fs laser micromachining is a versatile, practical, direct and efficient technique to fabricate 3D waveguide structures inside transparent dielectric materials.

The sign of the Δn of the local irradiation zone of the material depends on the type of the morphological change in the structure of the material. The first type of the morphological change is introduced by small damage produced inside the focal volume by fs laser irradiation which results as a smooth positive change on the local refractive

index [28]. Main mechanism behind such refractive index change is the increase in the material density inside the focal volume. As a result, this type of a Δn is usually observed at amorphous non-crystalline materials, since materials with crystalline structure have higher spatial order inside their lattice structure and harder to densify. It should be noted that the main disadvantage of this type of morphological change is that they can be easily removed even by only heating the sample, therefore they can degrade easily in high-power optical applications [26].

The other type of morphological change introduced by distinct damage tracks induced by fs laser irradiation inside the focal volume. This type of morphological change creates $\Delta n<0$ inside the local irradiated volume [29] and it has been reported for various different materials so far. Typically, this kind of a refractive index change corresponds to a decrease in the local material density, therefore amorphization inside the material structure. In addition, a stress-field surrounding the damage track is also created which increases the refractive index of the surroundings [30]. This feature can also be used to create a higher refractive index core when compared to the bulk of the material by simply inscribing subsequent damage tracks. This type of morphological change has also been studied comprehensively by using spectroscopic methods such as micro-Raman and can be summarized as follows: permanent damage on the lattice structure at the center of the damage track in the shape of sub-micron sized amorphous damage traces; compressed lattice structure surrounding the center of the damage track which consists thermally removable (thermally unstable) lattice defects; thermally stable and compressed lattice structure covering the whole damage track [31].

Although morphological changes and micromodifications inside the material depends on the material properties, process parameters have an important role one those aspects. The most important process parameters that are affecting the size and shape of the fabricated structures and the morphology of the irradiated material are pulse energy and pulse duration of the fs laser. Since formation of distinct damage tracks via fs laser irradiation involves several nonlinear processes, the peak power of the incident laser needs to be greater than a certain threshold value, which is also called as critical power [32]:

$$P_{crit} = \frac{3.77\ \lambda^2}{8\pi n_0 n_2} \tag{1.2}$$

where λ is the wavelength of the fs laser, n_0 is the linear refractive index of the sample and n_2 is the nonlinear refractive index of the sample. It should be noted that the peak power of the laser is a function of both the pulse energy and the pulse duration. It has been reported that for a fixed pulse duration, as the pulse energy increases to make the peak power greater than P_{crit}, the damage track becomes longer along the propagation direction and stress-field induced area becomes larger [28]. In contrast, decreasing pulse durations for a fixed pulse energy weakens the damage track since lower pulse durations increases the nonlinear absorption before the self-focused focal point.

Another parameter which affects the morphology and the geometry of the fabricated structure is the focusing condition of the irradiated fs laser, such as the NA and the depth of focus. NA typically determines the length of the damage track created along the propagation direction of the irradiated laser. An increase in the NA would increase the divergence of the laser after the focal point, leading to shorter damage tracks through the propagation distance since confocal parameter reduces with increasing NA. Depth of focus is the distance travelled by the laser beam inside the dielectric before it reaches to the focal point. It affects the processes such as absorption and dispersion, which may vary from material to material and need to taken into account. Moreover, both of the focusing condition parameters affect the spherical aberration introduced at the air/dielectric interface, which elongates the focal point along the propagation direction of the laser beam.

One process parameter apart from the laser and focusing parameters is the scan velocity of the beam (or sample). Scan velocity basically specifies the number of pulses penetrating each different focal point along the scanning direction. This number can be roughly estimated by the following formula [26]:

$$N = \frac{d\,f}{v} \tag{1.3}$$

where N is the number of pulses penetrating the same focal point, d is the spot diameter of the focused laser beam at the focal point, f is the repetition rate of the laser and v is the scan velocity. An increase in the number of pulses per focal point would increase the size of the modified volume and change the morphology of the fabricated structure; usually more pulses would increase the amount of micromodifications [26] and thus, refractive index contrast along the damage track. However, while choosing this

parameter, one should also take into account the time consumption during the processing as well as the optical losses may have occur during waveguiding due to the scattering.

Laser repetition rate is another key parameter that affects the result of the laser irradiation process for waveguide fabrication. Repetition rate distinguishes two different microprocessing regimes from one another; non-thermal and thermal microprocesses. In non-thermal processes, the time between two subsequent pulses is longer than the time needed for the heat produced on the processing volume to dissipate. Therefore, heat doesn't accumulate on the processing zone. On the other hand, in thermal processes, the time interval between two pulses is shorter than the time that heat needs to dissipate, therfore heat produced by every laser pulse overlaps with the previous pulse, which would turn the focal volume into a somewhat point heat source [33]. The critical repetition rate that determines the regime of the microprocessing can be found as [34]:

$$f_{crit} = \frac{\alpha}{d^2} \tag{1.3}$$

where α is the thermal diffusivity of the irradiated material and d is the diameter of the irradiated spot. As expected, the damage threshold of a material on thermal regime is lower than the nonthermal regime. Moreover, it has been reported that laser processing on thermal regime would result as a laser annealing effect on the locally processed area, leading to less defect concentration and better waveguiding characteristics [35].

Lastly, laser wavelength is not crucial on the process and not affecting the modifications in general, since the absorption process is nonlinear and not wavelength dependent. Typically, shorter wavelengths than those on the mid-infrared region would decrease the damage threshold of the material, and therefore increases the damaged volume surrounding the focal point. However, most of the commercially available fs lasers are on the mid-infrared region, therefore this aspect is negligible.

Fs laser written dielectric waveguides have various configurations, which depends on the geometry of the designed waveguide. Generally, fs laser written dielectric waveguide configurations are distinguished to two categories; Type I (positive refractive index change on the damage track) and Type II (negative refractive index change on the damage track) [26]. In the Type I category, the only waveguide configuration is directly written (single line) waveguides. In Type II, the configurations are stress-induced (double line) waveguides, depressed cladding waveguides and ridge waveguides. Detailed illustrations of the mentioned waveguide configurations can be seen in the below figure.

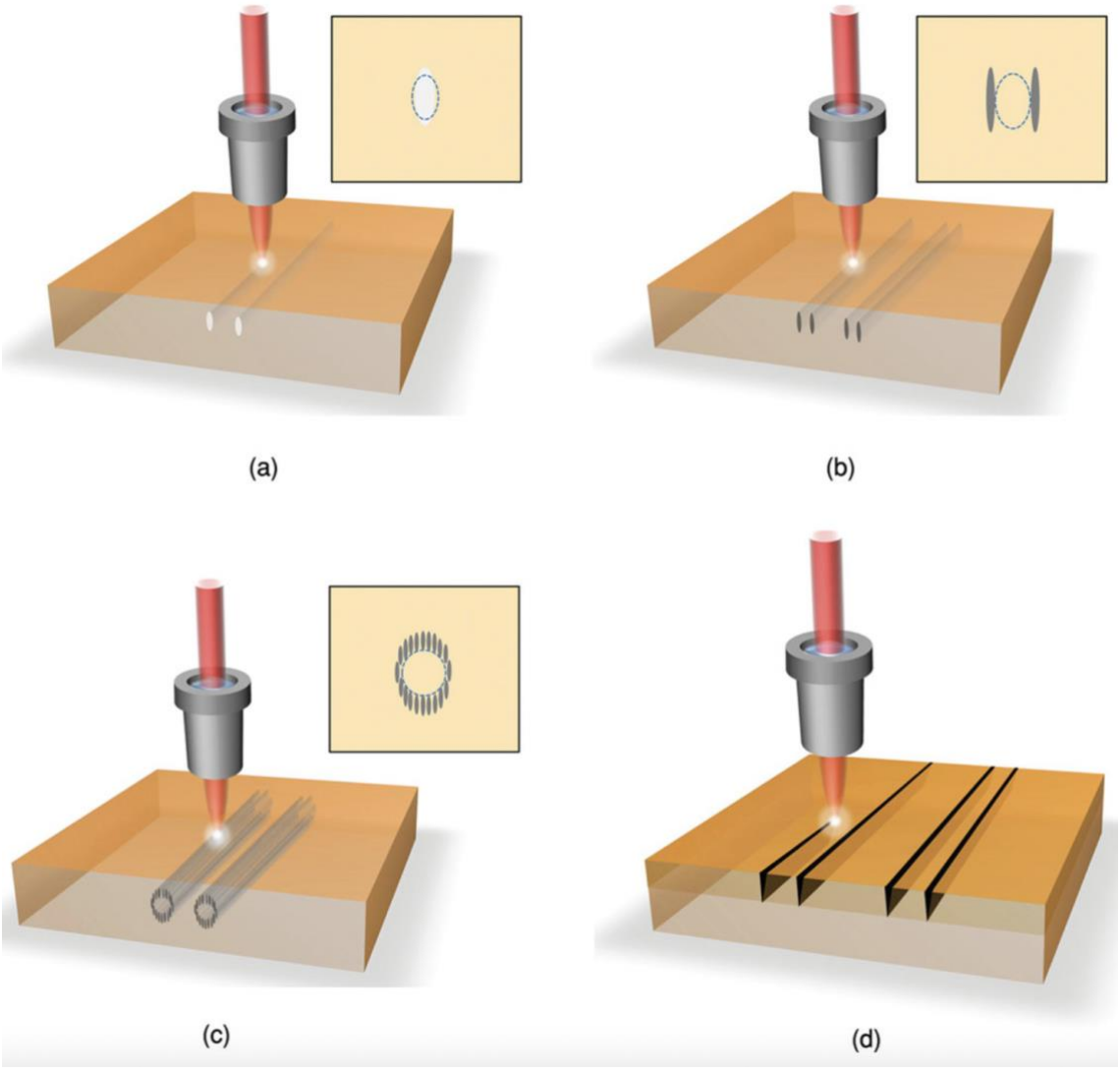

Figure 1.4: Illustration of fs laser writing of dielectric waveguides and their cross-sections for different waveguide configurations: (a) Single line (b) Double line (c) Depressed cladding d) Ridge waveguides (Sketches were taken from Ref. [26]).

As mentioned, single line waveguides have a positive refractive index change (Δn) relative to the bulk of the material throughout the written damage track, which acts as a waveguide core and the bulk of the material surrounding the track acts as a waveguide cladding. As previously discussed, this type of a change in the index induced by an increase in the local material density throughout the track, which is usually seen on materials with non-crystalline structure, such as glasses and limited only to a few crystalline materials, such as $LiNbO_3$ [36], ZnSe [37] and $Nd:YCa_4O(BO_3)_3$ [38]. The main advantage of this waveguide configuration comes from the simplicity during the fabrication process. Since the damage track itself acts as the core and the bulk of the

material acts as the cladding, the fabrication of the waveguide becomes a direct process, opens up possibilities to build rather complex waveguide devices such as directional couplers, Y-branches and waveguide arrays [27]. In addition, since the core of the waveguide in this configuration is rather small, it is suitable for single-mode guidance. The main disadvantage of this configuration also comes from the directness of the process; fs laser irradiation typically degrades the lattice features of the material, therefore any input light beam sent to the fabricated waveguide would have to propagate on a rather degraded region of the material, since the fs laser irradiated region itself directly acts as the waveguide core. Moreover, single line waveguides are structures which are thermally unstable, they can be easily degrade or even be removed by heat, thus, single line waveguides are usually not suitable for high-power guiding applications. The thermally unstable behaviour of the single line waveguides can be overcomed by multi-scan techniques, however, this would eliminate the directness of the process, which is the main advantage of the single line waveguides. Additionally, single line waveguides only support one polarization direction, limiting the guiding applications only demands 1D guidance [26]. An illustration of a fs laser written single line waveguide can be seen on Fig. 1.4 (a).

Double line waveguides generally consists of two parallel fs laser written tracks. As previously discussed, fs laser irradiation induces a negative refractive index change ($\Delta n<0$) in the locally modified track region due to the amorphization. In contrast, in the surrounding vicinity of the tracks, the index change is positive ($\Delta n>0$) due to the stress-induced densification of the lattice structure of the material. Therefore, with two parallel written tracks (usually with a length of 10-30 μm along the propagation direction) seperated by an optimal distance (usually 10-20 μm), double line waveguide configuration can be achieved with $\Delta n<0$ in the cladding region formed by the written tracks and $\Delta n>0$ in the core region. This configuration is especially advantageous in crystalline materials, since the core region of the material is not significantly affected from the laser irradiation; nonlinear and luminescence properties of the bulk are preserved. Compared to the single lines, double line waveguides are thermally stable and high-power guiding can be achieved using them. Additionally, depending on the material, guiding on two polarizations (transverse-electric (TE) and transverse-magnetic (TM)) is achievable since core of the waveguide has a higher refractive index than the bulk, providing a chance to use the bulk of the material as a cladding. However, the guiding on

both polarization directions may not be symmetric. It should be noted that, in general, formation mechanisms behind the Type II structures are better understood when compared with the Type I structures, making waveguide configurations belong to the Type II category more controllable. An illustration of a fs laser written double line waveguide can be seen on Fig. 1.4 (b).

In the category of Type II waveguides, another waveguide configuration is the depressed cladding waveguides. The waveguide core of this configuration consists completely bulk material and the cladding consists many low-refractive index tracks, induced by fs laser irradiation. The written tracks surrounds the waveguide core, forming a seemingly continuous circular optical wall which determines the waveguide cross-section and provides the guiding aspect of the waveguide. In theory, written tracks can form any geometrical shape but the general convention considers the circular shape since their coupling with other optical devices, such as fibers are the optimum. Typically, the waveguide core diameters are ranging from 20 μm to 150 μm and the distance between the tracks are around 2-4 μm, which makes this configuration rather versitile. Furthermore, from single-mode to multi-mode guiding is available from visible to mid-infrared regions in this configuration thanks to the availability of wide range of geometrical dimensions. The main advantage of this waveguide configuration is the availability of completely symmetrical 2D guidance. For most of the materials, the TE and TM mode guidance is identical, enabling efficient unpolarized pumping for applications such as waveguide lasers or frequency converters. The significant disadvantage of this configuration is the high amount of time consumption during the processing of the waveguide, since it usually consists many written tracks. An illustration of a fs laser written depressed cladding waveguide can be seen on Fig. 1.4 (c).

Instead of damage track formation, fs laser irradiation can also be used for etching, which is the fabrication mechanism behind the fs laser written ridge waveguides, a configuration belongs to the Type II category. Using a pre-fabricated planar waveguide substrate, ridge waveguides can be fabricated by etching the determined sections of the planar waveguides, forming an air-substrate interface which provides waveguiding. The main disadvantage of the ridge waveguides is the rough sidewalls produced during fabrication, which introduces additional optical losses to the structure. An illustration of a fs laser written ridge waveguide can be seen on Fig. 1.4 (d).

1.2 Diamond in Photonics

Diamond is a well known material for its strength, elegancy and scarcity. Its place in human history dates back to ancient Neolithic times for its use on polishing stone axes [39]. Using the well established techniques developed by the technological advances, such as chemical vapor deposition (CVD) and high pressur-high temperature (HPHT), diamonds as pristine as natural diamond can be grown in laboratory environment with various structures such as nano-, micro- and polycrystalline diamond, diamond wafers and single crystal diamond plates [39]. Availability of lab grown diamonds accelerated the research including diamond as well as opened up new research areas starring diamond. Interestingly, this ancient material is now under investigation to revolutionize the quantum information science thanks to its excellent optical/quantum-optical properties [39].

Diamond has a very large band gap which makes it both suitable for electronic applications as well as transparent from ultraviolet to mid-infrared range. High Raman gain coefficient of diamond makes it an excellent Raman gain medium [40], allowing applications including Raman scattering, such as diamond Raman lasers from visible to mid-infrared range [41, 42]. Additionally, diamond has a large linear and nonlinear refractive index (n_0=2.4, n_2 =1.3 x 10^{-19} m^2W^{-1}) [43]. Furthermore, diamond has an excellent thermal conductivity and low thermal expansion, allowing it to be able to operate on harsh conditions. Moreover, diamond is biocompatible and very stable in terms of its chemistry. Most importantly, diamond is a unique material for quantum applications since it hosts more than 500 optically active color centers, where some of those can be utilized as single photon sources at room temperature. The large bandgap of diamond allows us to recieve emission from those color centers without absorption. The ease to harness the quantum-optical properties of diamond made it an attractive material in the field of quantum information and communication.

Among 500 optically active color centers of diamond, only a few of them have been reported to have single photon emission at room temperature, which makes them single photon sources. The most researched color center among all is the nitrogen vacancy (NV) centers. NV centers have two distinct charge states; NV^0, the neutral charge state and NV^- the negative charge state. The NV^- and NV^0 states have zero-phonon emission lines at 637 nm and 575 nm, respectively, when excited optically with 532 nm green light. The

three-level energy band diagram of the NV centers has a unique feature; they have optical spin-polarization at room temperature, enabling optical spin readout applications. The optical spin readout from NV centers enables numerous metrological applications including diamond on nanoscale, such as high sensitivity magnetic field, temperature and strain measurements.

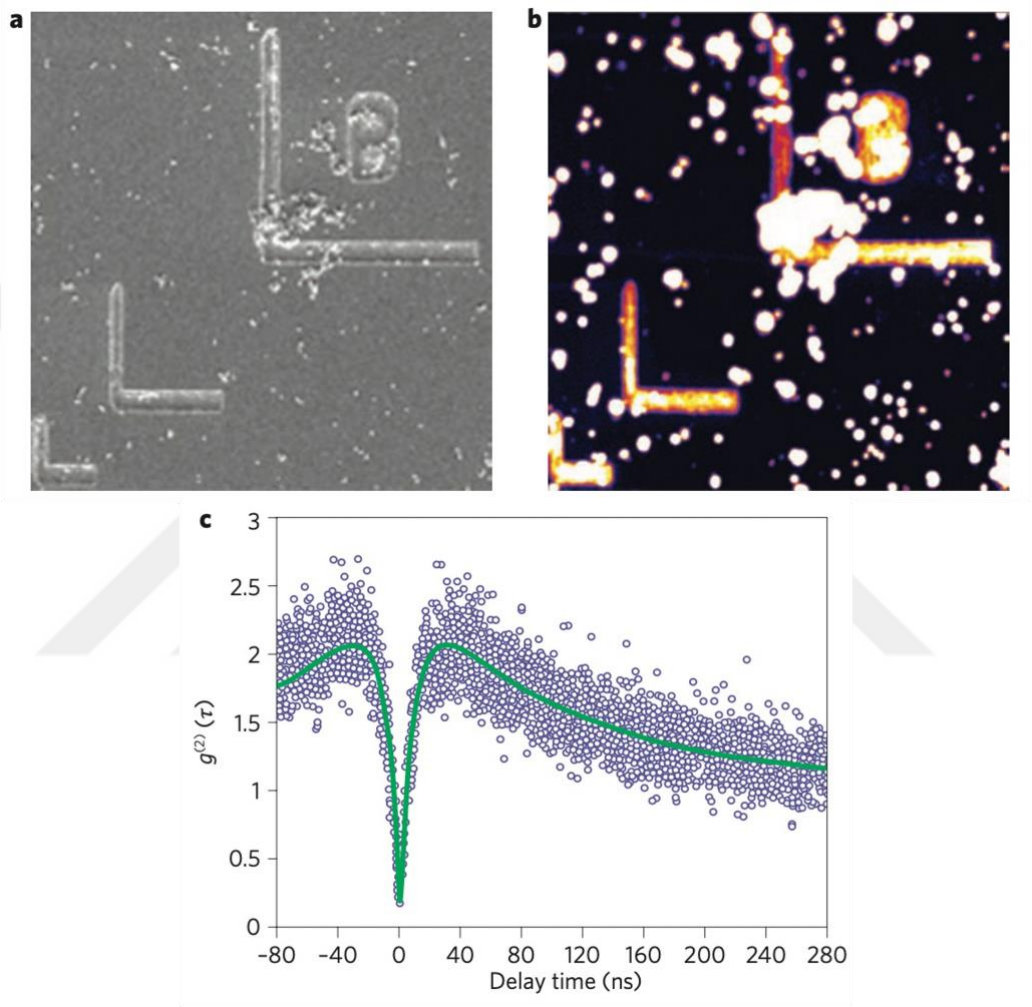

Figure 1.5: (a) Scanning electron microscopy and (b) confocal microscopy images of deposited nanodiamonds. Confocal microscopy image shows the single photon emission from NV centers as bright spots. (c) Second-order correlation function of a NV center from a nanodiamond (Figures and graph are taken from Ref. [44]).

The primary challange is to spatially link many NV centers in a way to enhance the emission of the NV centers and distinguish the well-defined electromagnetic modes. This inevitably requires the coupling of NV centers to optical cavities, especially waveguides. In such quantum sensing applications, optical waveguides play a crucial role, since they

can be used for addressing and spatially linking NV centers or for guiding fluorescence between different locations inside the diamond crystal.

In recent studies, the fs laser writing method has been employed to fabricate different types of optical waveguides inside diamond [45-55]. The potential of this method in fabricating three-dimensional waveguide structures has also been demonstrated [26]. Moreover, by positioning NV centers inside fs laser written double-line waveguides, potential quantum sensing platforms have been experimentally reported [48, 53, 55]. An example demonstration of a quantum magnetometry platform based on fs laser written diamond waveguides can be seen in the figure below.

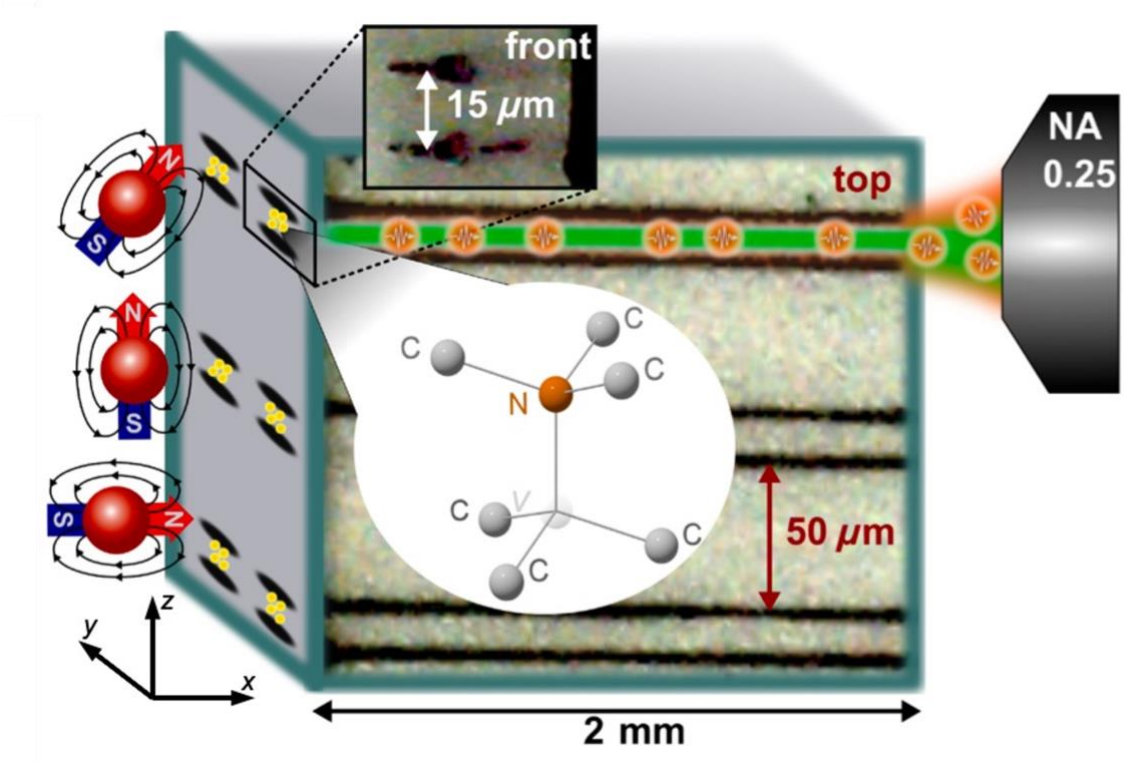

Figure 1.6: Illustration of a quantum magnetometry platform in the shape of a fs laser written double line waveguides inside a diamond sample (illustr1ation taken from Ref. [55]).

However, due to the graphitization of fs laser written domains, fabrication of low loss waveguides inside diamond remains a challenge and also a necessary step to fabricate efficient quantum sensors with high signal collection efficiency [56, 57]. Hence, understanding the effect of fs laser writing parameters on the amount of waveguide transmission losses as well as the degree of mode confinement (equivalently, the refractive index contrast) plays an important role in the development of high-quality

optical waveguides in diamond similar to waveguide structures fabricated in other dielectric media [26].

In this thesis, waveguides with different geometries and having various design parameters were fabricated in CVD grown diamond by employing fs laser writing. Detailed optical characterization of the waveguides with different design parameters was performed at the wavelength of 633 nm. Results clearly revealed the important dependence of propagation loss and refractive index contrast on the design parameters of the waveguides. In previous studies, the reported lowest propagation loss of femtosecond laser written diamond waveguide was at the level of 4.20 dB/cm [48]. To the best of our knowledge, the propagation loss levels of 2.05 dB/cm and 1.20 dB/cm, obtained in this study with circular depressed cladding and half-ring waveguides, respectively, are the lowest propagation loss values reported so far for fs laser written diamond waveguides.

Chapter 2:
EXPERIMENTS AND RESULTS

2.1 Waveguide Fabrication Setup

In the experiments, waveguides were written inside a 3 x 5 x 6.7 mm sized, single crystal, CVD grown diamond sample. Crystal growth occurred along the [100] crystallographic direction (Appsilon B.V.). All of the facets of the sample were pre-polished for waveguide writing experiments. Fig. 2.1(a) includes a sketch of the waveguide writing setup which shows the orientation of the diamond sample and defines the writing parameters of the waveguides. A commercial, regeneratively amplified fs Ti3+:Sapphire laser (MKS Newport-Spectra Physics Spitfire Ace) was utilized in waveguide writing experiments. The laser generated 120 fs pulses at the central wavelength of 800 nm and at a pulse repetition rate of 1 kHz. Laser pulses were focused to a depth of approximately 100 μm below the top surface of the diamond sample by using a 40X objective (Olympus Plan-N, Numerical Aperture (NA)=0.65). Precision writing of the waveguides was achieved by using a computer controlled 3-D stage (Newport μFab). Femtosecond laser writing was performed along the [100] direction of the diamond crystal.

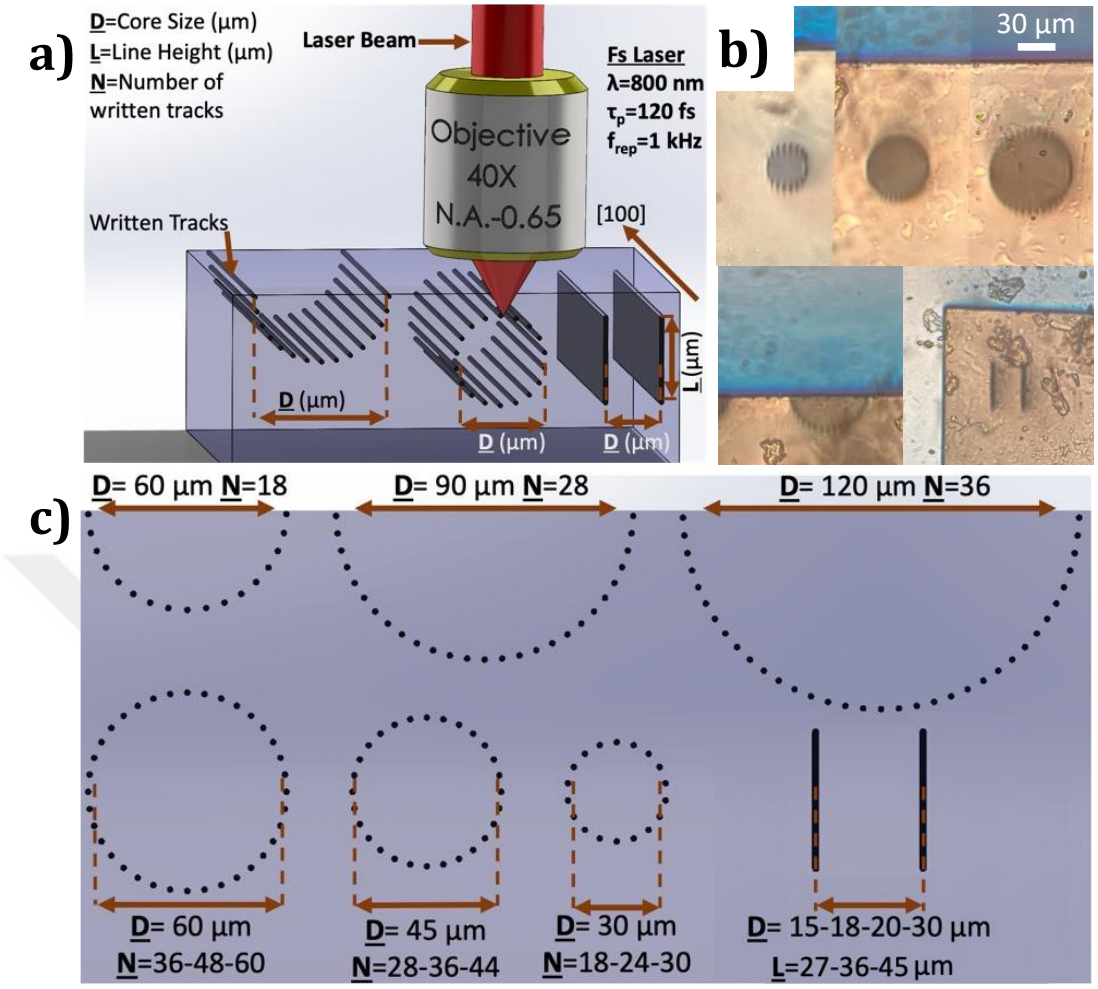

Figure 2.1: (a) Sketch of the microfabrication setup for waveguide writing, including cross-sectional sketches of a half-ring waveguide, circular depressed cladding waveguide, and a double-line waveguide along with the definition of the waveguide design parameters: Core size "D", line height "L" and number of written tracks "N". (b) Optical microscopy images of the fabricated waveguides with design parameters of (top row, left to right): D = 30 µm and N =18; D = 45 µm and N = 28; D = 60 µm and N =36 (circular depressed cladding waveguides); (bottom row, left) D = 60 µm and N =18 (half-ring waveguide); and (bottom row, right) D = 30 µm and L = 45 (double-line waveguide). (c) Specific design parameters of the waveguides fabricated in this study.

2.2 Fabricated Waveguides

Optical microscopy images of some of the written waveguides taken from the input facet can be seen in Fig. 2.1(b). During the fabrication of the circular depressed cladding

waveguides, the incident pulse energy, energy fluence, and scan velocity were set to 100 nJ, 2 J/cm^2, and 0.4 mm/s, respectively. It should be noted that the pulse energy and scan velocity parameters were optimized by several waveguide fabrication and propagation loss characerization trials. In the below Fig. 2.2, waveguides fabricated with pulse energies ranging from 285 to 100 nJ and scan velocities from 0.2 to 0.6 mm/s can be seen. All those waveguides with different parameters were inferior when compared to the top rightmost waveguide in Fig. 2.1(b), both in terms of optically and visually.

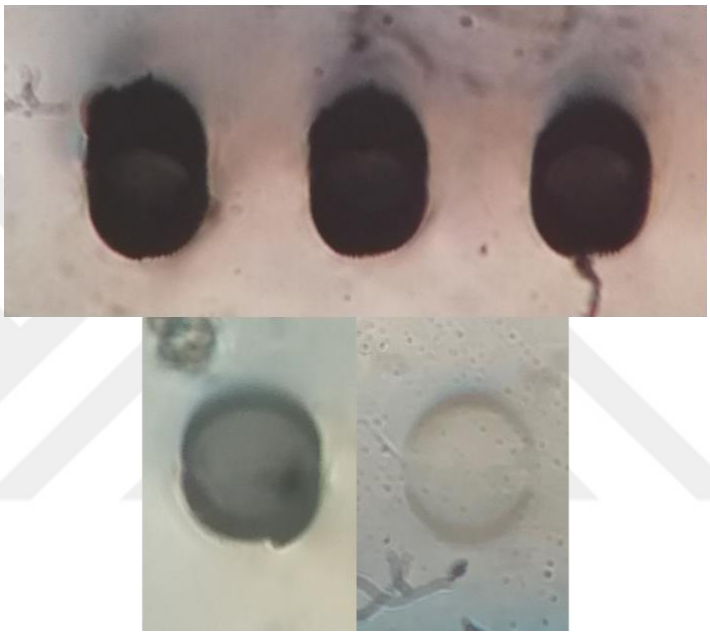

Figure 2.2: Optical microscopy images of several waveguides having the same geometry with different fabrication parameters: (top row, left to right) pulse energy = 285 nJ and scan velocity = 0.2 mm/s, pulse energy = 215 nJ and scan velocity = 0.2 mm/s, pulse energy = 140 nJ and scan velocity = 0.2 mm/s; (bottom row, left to right) pulse energy = 100 nJ and scan velocity = 0.2 mm/s, pulse energy = 100 nJ and scan velocity = 0.6 mm/s.

In the case of depressed claddings, both circular and half-ring waveguides were fabricated. The only distinguishing aspect of the half-rings from the circular depressed claddings was that they were written directly below the top surface, whereas the latter were written at a depth of 100 μm beneath the surface. Nine different circular depressed cladding waveguides were fabricated, with core sizes of D = 30, 45 and 60 μm and with

the number *N* of written tracks ranging from 18 to 60. See Fig. 2.1(c) for a complete list of the waveguides fabricated in this study. For the half-rings, 3 waveguides were fabricated with *D* = 60, 90, and 120 μm and with corresponding *N* values of 18, 28, and 36. While fabricating the double-lines, the same incident pulse energy and fluence were used with a scan speed of 0.1 mm/s. Note that during the fabrication of double-lines, the line height *L* was controlled by writing different number of tracks along the vertical direction of the crystal (see Fig. 2.1(a)). With the pulse fluence of 2 J/cm2 and scan speed of 0.1 mm/s used during the fabrication of double-lines, tracks with a height of approximately *L* = 9 μm were created along the vertical direction. Thus, by consecutively writing 3 to 5 tracks along the vertical direction, 12 different double-line waveguides with core sizes of *D* = 15, 18 20, and 30 μm and with line heights of *L* = 27, 36, and 45 μm were successfully written inside the bulk of the crystal. The design parameters for all fabricated waveguides are summarized in Fig. 2.1(c). Note that the fabrication parameters used in this study were optimized by minimizing the loss arising from graphitization during fs laser writing and at the same time, by maintaining sufficient confinement within the waveguides. When compared with a previous study described in Ref. [51], even though the N.A. value used here is lower than those in the reported study, no discontinuity was observed here across the fs laser written tracks. This is possibly due to the fact that the operation wavelength (515 nm), pulsewidth (230 fs), and repetition rate (1 MHz) of the laser used in Ref. [51] are quite different than those used in this study (wavelength of 800 nm, pulsewidth of 120 fs, and repetition rate of 1 kHz), resulting in a different fabrication regime.

2.3 Waveguide Characterization

After the writing experiments, optical guiding characteristics of the waveguides were investigated. A sketch of the setup for waveguide characterization is shown in Fig. 2.3(a). Characterization was performed by using a commercial He-Ne laser operating at 633 nm, close to the peak wavelength of fluorescence for NV centers [58]. The laser was coupled to the waveguides by using an input converging lens (L1) and guiding was obtained for each waveguide. The spot radius (1/e2) of the He-Ne laser beam was measured as 1.10 mm at the location of L1. The guided beam exiting from the output facet of the diamond crystal was collimated and imaged with an aspheric lens (L2) which had an effective focal

length of f = 6 mm. As an example, Figures 2.3(b)-(e) show the images of the exit facet of a circular depressed cladding (D = 45 μm and N = 28) and a half-ring (D = 90 μm and N = 28) waveguide for the cases of no coupling and optimized coupling. In addition, the far-field spatial intensity profile of the guided beam from the same waveguides can be seen in Figs. 2.3(f) and 2.3(g). Figs. 2.3(h) and 2.3(i) show the top view images of the cases of no coupling and optimum coupling for the circular depressed cladding waveguide having D = 45 μm and N = 28.

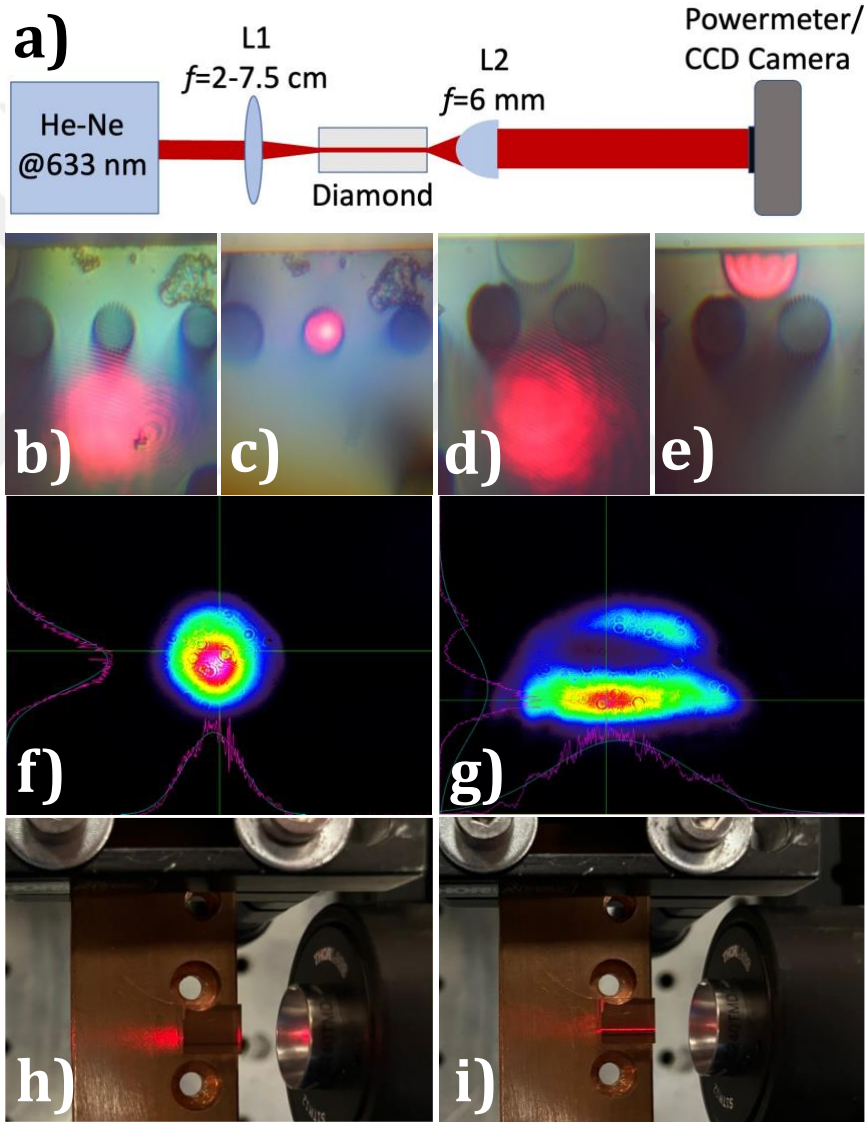

Figure 2.3: (a) Optical characterization setup of the diamond waveguides. Images of the exit facet of the circular depressed cladding waveguide with core size D = 45 μm and

number of written tracks N = 28 for the cases of (b) no coupling and (c) optimized couplin g. Images of the exit facet of the half-ring waveguide with D = 90 μm and N = 28 for the cases of (d) no coupling and (e) optimized coupling. Far-field spatial intensity profile of the guided beam from (f) the circular depressed cladding waveguide with D = 45 μm and N = 28, and (g) half-ring waveguide with D = 90 μm and N = 28. Top view images for the cases of (h) no coupling and (i) optimum coupling for the circular depressed cladding waveguide having D = 45 μm and N = 28.

In the measurement of the waveguide propagation losses, in order to correct for the Fresnel losses, propagation loss of each waveguide was determined by comparing the power transmission of the waveguide with the bulk transmission of the crystal. In particular, the diamond crystal was first positioned on a 3-D translation stage and the power $P_{coupled}$ of the guided beam was measured after the optimization of waveguide coupling. Here, care was taken to block the uncoupled portion of the transmitted laser beam in the far field by using an iris. Next, the focused laser beam was uncoupled from the waveguide by translating the diamond crystal to measure the transmitted power P_{bulk} through the bulk of the sample. The propagation loss of the waveguide in units of dB/cm was then computed by using the equation:

$$Propagation\ Loss = \frac{10\log\left(\frac{P_{bulk}}{P_{coupled}}\right)}{L} \tag{2.1}$$

In Eq. (1), L is the length of the sample. It should be noted that no significant polarization dependence was observed from the circular depressed claddings, since they have a symmetric distribution of refractive index contrast. Figure 2.4(a) shows the measured variation of the propagation loss as a function of the number N of written tracks for the circular depressed cladding waveguides. In terms of propagation loss, the best performing circular depressed cladding waveguide had the parameters of D = 60 μm and N = 36. On the other hand, the highest propagation loss was observed for the waveguide with D = 30 μm and N = 30. Data displayed in Fig. 2.4(a) show that the propagation losses vary directly with the number N of written tracks and inversely with the core size D. In the case of written tracks, it has been shown in previous studies [57] that fs laser writing causes the formation of graphite-rich regions, which introduce losses for the guided mode

due to optical absorption in graphite. In the case of the dependence on core size, this is due to the increase in the size of the unmodified core region as the core diameter increases [20]. Hence, the trends observed in Fig. 2.4(a) may be qualitatively explained based on these effects.

In the case of circular depressed cladding waveguides, depressed double-ring and triple-ring waveguide configurations were also fabricated and characterized by measuring their propagation losses. Fig. 2.4(b) shows the optical microscope images of fs laser written triple-, double-, and single-ring circular depressed cladding waveguides. Note that the same fabrication parameters were used during the fabrication of the double and triple-ring waveguides as in the case of single-ring circular depressed cladding waveguides. To fabricate the depressed double-ring waveguide, the depressed cladding waveguide with D = 30 µm and N = 24 was first written and on top of it, another concentric ring with D = 45 µm and N = 36 was fabricated to form the second cladding. For the depressed triple-ring waveguide, a third concentric ring with D = 60 µm and N = 48 was fabricated on top of the double-ring structure with D = 45 µm and N = 36. The propagation losses from depressed single-, double-, and triple-ring waveguides was 11.10, 12.70, 13.30 dB/cm, respectively. As it can be seen, increasing the number of cladding rings resulted in more propagation loss, which is due to the increased graphitization of the waveguide structure.

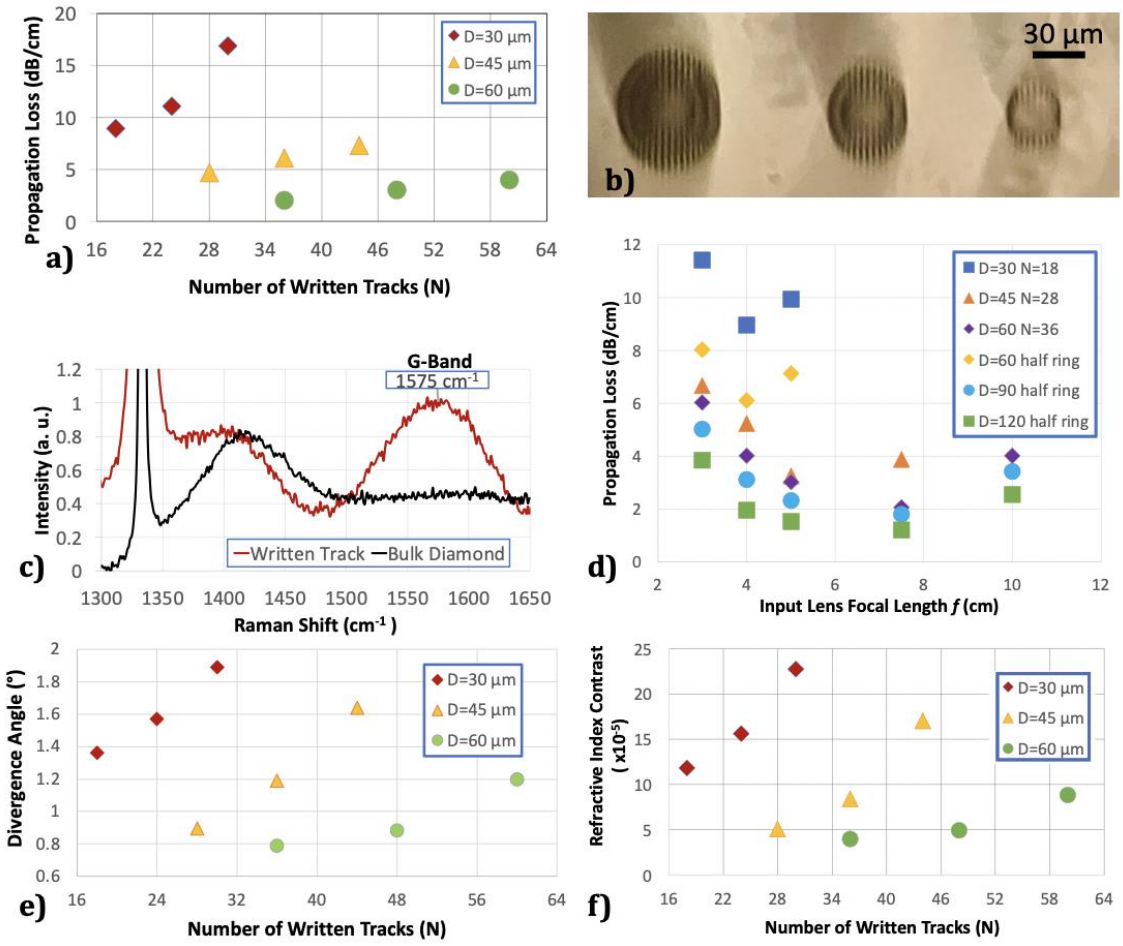

Figure 2.4: (a) Measured variation of the propagation loss as a function of the number N of written tracks for circular depressed cladding waveguides with different core sizes D. (b) From left to right: optical microscopy images of fs laser written triple-, double-, and single-ring circular depressed cladding waveguides. (c) Raman spectra taken from bulk diamond and a written track (normalized with respect to the intensity of the G-band). (d) Measured variation of the propagation loss as a function of input lens focal length. (e) Measured divergence angle of the laser beam exiting each of the fabricated waveguides as a function of N for waveguides with different D. (f) Measured refractive index contrast of each circular depressed cladding waveguide as a function of N for waveguides with different D.

In addition, by using the same characterization setup, we were able to obtain guiding in half-ring waveguides with core sizes of D = 60, 90 and 120 µm (see Figs. 2.1(b) and 2.3(e)). The measured propagation losses were 6.18, 1.87, and 1.20 dB/cm, respectively.

To support the trends shown in Fig. 2.4(a), we further examined the structure of the written tracks with a Raman microscope (Renishaw inVia Raman). A 532 nm laser was used as the excitation source and was focused with a 100X objective on the written tracks. The Raman spectra of a written track as well as of bulk diamond with its corresponding 1332 cm^{-1} Raman peak are shown in Fig. 2.4(c). The corresponding Raman peak of graphite (G-Band) can be clearly seen at 1575 cm^{-1} for the written track region. We note here that scattering from written tracks can also contribute to transmission losses in the waveguides. Our Raman spectrum measurements suggest that a portion of this loss could be attributed to graphitization arising from fs laser writing.

Note that, to reduce the propagation losses due to the mode mismatch between the input beam and the waveguide mode, the focal length *f* of the input coupling lens (L1) was varied for the waveguides with different core sizes. Fig. 2.4(d) shows the variation of the propagation loss of half-ring and circular depressed cladding waveguides for different values of *f*. The procedure used in this experiment is similar to the loss analysis described in Ref. [59]. Note that, for the case of circular depressed cladding waveguides, only the specific configuration (with a particular *N* value) having the lowest measured loss is shown. Also note that as the core size of the waveguide increases, the corresponding value of the optimum focal length also increases as shown Fig. 2.4(d). Due to the different core sizes, the lowest propagation loss of each waveguide is obtained at a different optimum focal length, as expected. Beyond the optimum focal length, the propagation loss starts to increase again due to the increase in mode mismatch. Thus, from the data displayed in Fig. 2.4(d), the optimum focal length was determined as f = 4.0, 5.0, and 7.5 cm for the depressed cladding waveguides with core sizes of D = 30 µm (and 60 µm half-ring), 45 µm (and 90 µm half-ring), and 60 µm (and 120 µm), respectively.

To ensure that all cases of coupling remain within the regime of waveguiding, the Rayleigh range inside the diamond crystal was further calculated for each input lens. Here, the beam waist of the focused beam w_2 was first determined by using [60]:

$$\frac{w_1}{w_2} \approx \frac{f}{z_1} \tag{2.2}$$

where z_1 is rayleigh range of incident beam, f is the focal length of the input lens and w_1 is the beam waist before the input lens. The corresponding Rayleigh range z_R inside diamond was calculated by using the formula:

$$z_R = \frac{n\pi w_2^2}{\lambda} \tag{2.3}$$

In Eq. (2.3), n is the refractive index of the medium (n = 2.4 for diamond) [39] and λ is the wavelength of the laser. Note that, L/z_R (L = crystal length = 6.7 mm) comes to L/z_R =18.6, 10.5, 6.7 and 3.0 for the focal lengths of f = 3.0, 4.0, 5.0, and 7.5 cm, respectively. This indicates that even in the case of f = 7.5 cm, the crystal length L remains reasonably large in comparison with the Rayleigh range z_R and beam propagation occurs predominantly in the waveguiding regime.

Furthermore, the Δn between the fs laser written tracks and the guiding region (core) was investigated as a function of N and D for circular depressed cladding waveguides. By using the step index waveguide approximation, Δn was determined from [20, 61]:

$$\Delta n \approx \frac{\sin^2 \theta}{2n} \tag{2.4}$$

In Eq. (2.4) above, θ is the divergence angle, n is the refractive index of the medium and Δn is the refractive index contrast produced by fs laser writing. The divergence angle was experimentally determined by using the knife-edge method, where the spotsize of the exiting beam was measured after the waveguide as a function of position at 5-mm intervals. The detailed information on the measured spot sizes can be found in the Appendix A. Experimentally determined divergence angle of each waveguide is plotted as a function of N in the Fig. 2.4(e). As it can be seen, the divergence angle of the beam exiting the waveguide is increases directly with N and inversely with D. Using the divergence angles shown in Fig. 2.4(e), the Δn of each waveguide is determined according to the Eq. (2.4) and plotted as a function of N and D in Fig. 2.4(f). The largest Δn value of 22.70×10^{-5} was measured for the waveguide with D = 30 μm and N = 30, whereas the smallest value (3.90×10^{-5}) was obtained for the waveguide with D = 60 μm and N = 36. In Fig. 2.4(f), the measured Δn of each circular depressed cladding waveguide was plotted as a function of the number of written tracks N for waveguides with different core sizes D. The results show that Δn increases with increasing number of written tracks and decreases as the core size increases. Previous studies show that fs laser written tracks introduce a decrease in the refractive index around the modified track regions in diamond [49]. Hence, the trends observed in Fig. 2.4(f) are as expected since the ratio of the modified region to the unmodified region increases by reducing the core size and by

increasing the number of written tracks. It should be noted that the divergence angle and the Δn of the fabricated waveguides follow the same trends with respect to varying N and D, which is expected since an increase in Δn would increase the NA of a waveguide and therefore the divergence angle of the exiting beam. In addition, Δn of the circular, depressed double-ring and triple-ring waveguides was determined by using the same method and found as 16.30×10^{-5} and 17.70×10^{-5}, respectively. These are higher than the Δn value of 15.60×10^{-5} of their single-ring counterpart (D = 30 μm and N = 24). It should be noted that in the previous studies, Δn values as high as 3.0×10^{-3} could be achieved [49] in diamond, which are significantly higher than the results obtained here. This is possibly due to the fact that the waveguide fabrication regime in Ref. [49] was completely different (laser wavelength=515 nm, pulsewidth=230 fs, and pulse repetition rate=1 MHz) from what was used in the current study, as noted before. In addition, the wall seperation in [9] was as low as 13 μm, which is expected to increase the refractive index contrast significantly.

The mode-field diameter (MFD) of the circular depressed cladding waveguides was further estimated by using the empirical formula for step-index fibers given by [62]:

$$MFD = 2a\left(0.65 + \frac{1.619}{V^{1.5}} + \frac{2.879}{V^{6.0}}\right) \tag{2.5}$$

In Eq. (2.5) above, a is the waveguide core radius and V is the V-number, which can be calculated from [60]:

$$V = \frac{2\pi a}{\lambda}\sqrt{n_{core}^2 - n_{cladding}^2} \tag{2.6}$$

In Eq. (6) above, n_{core} is the refractive index of the core region of the waveguide (n=2.4 for diamond) and $n_{cladding}$ is the refractive index of the cladding region, which is found by using the experimentally determined index contrast ($n_{cladding} = n_{core} - \Delta n$), as described above. The other parameters in Eq. (2.6) were defined before. Fig. 2.5(a) shows the variation of the MFD as a function of the number N of written tracks for each of the fabricated circular depressed cladding waveguides with a given core size D. Note that as N increases, the confinement increases and the MFD decreases as expected.

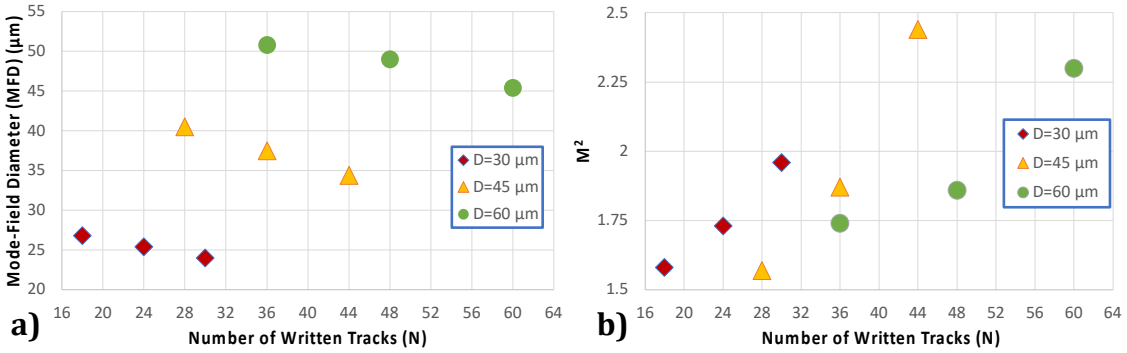

Figure 2.5: Calculated (a) mode-field diameter (MFD) and (b) M2 parameter as a function of the number N of written tracks for each of the fabricated circular depressed cladding waveguides with a core size of D.

In addition, the MFD and the measured divergence angle of the circular depressed cladding waveguides were used to calculate the M^2 parameter of the output beam by using the relation [60]:

$$M^2 = \frac{\pi\theta(MFD)}{2\lambda} \tag{2.7}$$

In Eq. (7), θ is the divergence half-angle, *MFD* is the mode-field diameter. Fig. 2.5(b) shows the Calculated M^2 parameter as a function of *N* for each of the fabricated circular depressed cladding waveguides with a core size of D.

In the last set of experiments, the propagation loss of double-line waveguides was measured and plotted as a function of line height *L* in Fig. 2.6. During the measurements, similar to the depressed claddings, to reduce the propagation losses, the focal length *f* of the input coupling lens L1 was chosen as *f* = 2, 3, and 4 cm for the double-line waveguides with a core size of *D* = 15, 18 (and 20), and 30 µm, respectively. Note that the measurements were done with TM polarized light since the propagation loss of double-lines is highly polarization dependent [26]. The lowest propagation loss of 4.84 dB/cm was obtained with the double-line waveguide having *D* = 30 µm and *L* = 45 µm. On the other hand, the highest loss of 16.79 dB/cm was obtained with the waveguide having *D* = 15 µm and *L* = 45 µm. The measured data show that at a fixed line height *L*, as the core size increases for the double lines, propagation losses decrease, which agrees with the previous results obtained with circular depressed cladding waveguides in this study. When the propagation losses are examined at a fixed *D* value as a function of the line

height *L*, three different trends can be seen for waveguides having *D* = 15 µm, *D* = 18 µm, and *D* = 20, 30 µm. In the cases of waveguides having *D* = 20 and 30 µm, the propagation losses vary inversely with the line height *L*. For the *D* = 15 µm waveguides, the observed trend is opposite. Lastly, no significant change was observed in the propagation loss for the case with *D* = 18 µm. This is primarily because two competing effects occur as *L* is varied. In the first effect, as the line height L of a waveguide is increased while keeping the core size *D* constant, the geometry of the waveguide becomes more favorable for supporting the TM polarization due to the increased aspect ratio (*L*/*D*) of the waveguide. Since the input light is TM polarized in the case of double-lines, increasing *L* causes a decrease in the propagation loss. In the second effect, increasing *L* means an increase in the number of written tracks along the vertical direction of the crystal, leading to more graphitization in the vicinity of the written tracks and higher propagation loss due to graphite absorption. Thus, in the case of waveguides having *D* = 20 and 30 µm, the first effect is dominant, whereas for *D* = 15 µm the second effect dominates. For the waveguides with *D* = 18 µm, the two effects approximately cancel each other, leading to no significant dependence on *L*.

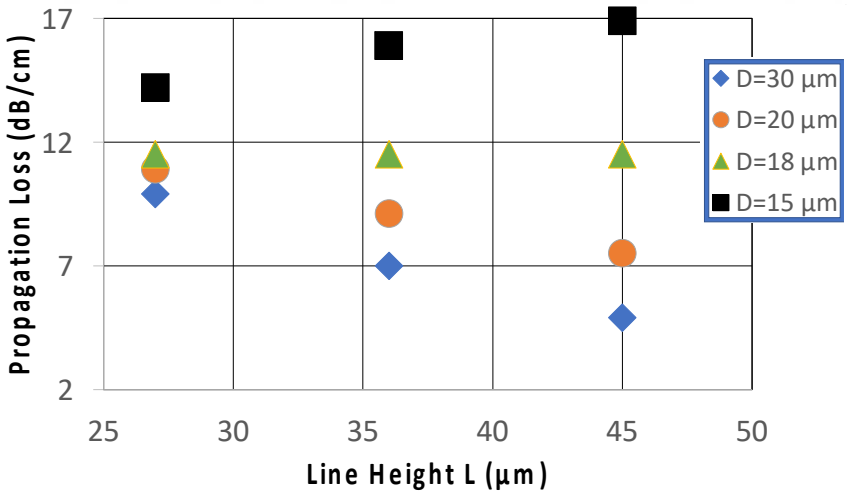

Figure 2.6: Measured propagation loss as a function of the line height L for double-line waveguides with different D.

Chapter 3:
CONCLUSION

In conclusion, we have experimentally investigated the effect of the design parameters on the propagation loss and the refractive index contrast of fs laser written waveguides in a CVD grown diamond crystal. The obtained experimental results show that the propagation loss of the fs laser written waveguides decreases as the core size increases and as the number of written tracks decreases. Similarly, the refractive index contrast between the core and the written tracks showed the same trend as the propagation loss. Therefore, varying the design parameters for the sake of minimizing the loss of the waveguide also reduces the ability of the waveguide to confine the propagating mode. With regard to the experimental results, refractive index contrasts ranging from 3.90x10-5 to 22.70x10-5 were obtained for depressed cladding waveguides. Moreover, double- and tripple-ring waveguide configurations of the circular depressed cladding waveguides resulted in more beam confinement but at the cost of more propagation losses. Overall, we were able to obtain propagation losses as low as 2.05 dB/cm and to 1.20 dB/cm by utilizing circular depressed cladding and half ring configurations, respectively. In addition, propagation loss of 4.84 dB/cm was obtained with double-line waveguides, which is within the range of loss values reported so far for CVD grown diamond [45, 46, 48]. Double-line configuration provided more spatial confinement and smaller mode field diameters but, again, more losses were encountered due to graphitized regions. Table 1 summarizes the waveguide configurations and obtained loss values reported in previous studies involving fs laser written diamond waveguides [6-12]. To our knowledge, the propagation loss values obtained with our circular depressed cladding and half-ring waveguides are the lowest reported to date for fs laser written waveguides in diamond. Furthermore, among the waveguide geometries investigated in this study, half-ring waveguides appear to be the most promising in terms of low loss propagation and we forsee that they can have important potential applications in linking NV centers in diamond for quantum sensing/communication applications.

Table 3.1: Summary of waveguide configurations and obtained loss values reported in previous studies with fs laser written diamond waveguides.

Reference	Waveguide configurations	Loss
Present Study	Double-line, circular depressed cladding, double- and triple-ring, half-ring	As low as 1.20 dB/cm
[45]	Double-line	16.00 dB/cm
[46]	Double-line, circular depressed cladding and Y-branch	As low as 7.90 dB/cm
[48]	Double-line	4.20 dB/cm
[49]	Double-line	Not specified
[52]	Circular depressed cladding	As low as 11.60 dB/cm
[53]	Double-line	6.00 dB insertion loss
[55]	Double-line	6.95 dB insertion loss

BIBLIOGRAPHY

[1] T. H. Maiman, "Stimulated Optical Radiation in Ruby," *Nature*, vol. 187, no. 4736, pp. 493-494, 1960/08/01 1960, doi: 10.1038/187493a0.

[2] C. R. Giuliano, "Laser-Induced Damage to Transparent Dielectric Materials," *Applied Physics Letters*, vol. 5, no. 7, pp. 137-139, 1964.

[3] J. Hecht, "Short history of laser development," *Optical Engineering*, vol. 49, no. 9, p. 091002, 2010. [Online]. Available: https://doi.org/10.1117/1.3483597.

[4] J. de Damborenea, "Surface modification of metals by high power lasers," *Surface and Coatings Technology*, vol. 100-101, pp. 377-382, 1998/03/01/ 1998, doi: https://doi.org/10.1016/S0257-8972(97)00652-X.

[5] R. F. Wood, C. W. White, and R. T. Young, "Chapter 1 Laser Processing of Semiconductors: An Overview," in *Semiconductors and Semimetals*, vol. 23, R. F. Wood, C. W. White, and R. T. Young Eds.: Elsevier, 1984, pp. 1-41.

[6] R. R. Gattass and E. Mazur, "Femtosecond laser micromachining in transparent materials," *Nat Photonics*, vol. 2, no. 4, pp. 219-225, 2008/04/01 2008, doi: 10.1038/nphoton.2008.47.

[7] D. Du, X. Liu, G. Korn, J. Squier, and G. Mourou, "Laser-induced breakdown by impact ionization in SiO2 with pulse widths from 7 ns to 150 fs," *Applied Physics Letters*, vol. 64, no. 23, pp. 3071-3073, 1994, doi: 10.1063/1.111350.

[8] A. P. Joglekar, H. Liu, G. J. Spooner, E. Meyhöfer, G. Mourou, and A. J. Hunt, "A study of the deterministic character of optical damage by femtosecond laser pulses and applications to nanomachining," *Applied Physics B*, vol. 77, no. 1, pp. 25-30, 2003/08/01 2003, doi: 10.1007/s00340-003-1246-z.

[9] R. Boyd, "Nonlinear Optics 2nd edn (Amsterdam: Academic)," 2003.

[10] B. C. Stuart, M. D. Feit, S. Herman, A. M. Rubenchik, B. W. Shore, and M. D. Perry, "Nanosecond-to-femtosecond laser-induced breakdown in dielectrics," *Physical Review B*, vol. 53, no. 4, pp. 1749-1761, 01/15/ 1996, doi: 10.1103/PhysRevB.53.1749.

[11] A. Vogel and V. Venugopalan, "Mechanisms of pulsed laser ablation of biological tissues," *Chemical reviews*, vol. 103, no. 2, pp. 577-644, 2003.

[12] J. B. Ashcom, R. R. Gattass, C. B. Schaffer, and E. Mazur, "Numerical aperture dependence of damage and supercontinuum generation from femtosecond laser pulses in bulk fused silica," *J. Opt. Soc. Am. B*, vol. 23, no. 11, pp. 2317-2322, 2006/11/01 2006, doi: 10.1364/JOSAB.23.002317.

[13] N. Bloembergen, "Laser-induced electric breakdown in solids," *IEEE Journal of Quantum Electronics*, vol. 10, no. 3, pp. 375-386, 1974, doi: 10.1109/JQE.1974.1068132.
[14] M. Will, S. Nolte, B. N. Chichkov, and A. Tünnermann, "Optical properties of waveguides fabricated in fused silica by femtosecond laser pulses," *Appl. Opt.*, vol. 41, no. 21, pp. 4360-4364, 2002/07/20 2002, doi: 10.1364/AO.41.004360.
[15] E. N. Glezer and E. Mazur, "Ultrafast-laser driven micro-explosions in transparent materials," *Applied Physics Letters*, vol. 71, no. 7, pp. 882-884, 1997, doi: 10.1063/1.119677.
[16] Y. R. Shen, "Self-focusing: Experimental," *Progress in Quantum Electronics*, vol. 4, pp. 1-34, 1975/04/01/ 1975, doi: https://doi.org/10.1016/0079-6727(75)90002-6.
[17] R. R. Alfano and S. L. Shapiro, "Observation of Self-Phase Modulation and Small-Scale Filaments in Crystals and Glasses," *Physical Review Letters*, vol. 24, no. 11, pp. 592-594, 03/16/ 1970, doi: 10.1103/PhysRevLett.24.592.
[18] D. Kip, "Photorefractive waveguides in oxide crystals: fabrication, properties, and applications," *Applied Physics B: Lasers & Optics*, vol. 67, no. 2, 1998.
[19] T. Suhara and M. Fujimura, *Waveguide nonlinear-optic devices*. Springer Science & Business Media, 2003.
[20] Y. Morova, M. Tonelli, and A. Sennaroglu, "Fabrication of femtosecond laser written depressed-cladding waveguides in Tm3+:BaY2F8 crystal and laser operation near 2 mu m," (in English), *Optical Materials*, vol. 126, Apr 2022, doi: ARTN 112121
10.1016/j.optmat.2022.112121.
[21] Y. Su, Y. Zhang, C. Qiu, X. Guo, and L. Sun, "Silicon photonic platform for passive waveguide devices: Materials, fabrication, and applications," *Advanced Materials Technologies*, vol. 5, no. 8, p. 1901153, 2020.
[22] W. Sohler *et al.*, "Integrated Optical Devices in Lithium Niobate," *Opt. Photon. News*, vol. 19, no. 1, pp. 24-31, 2008/01/01 2008, doi: 10.1364/OPN.19.1.000024.
[23] W. Bolaños *et al.*, "Continuous-wave and Q-switched Tm-doped KY(WO4)2 planar waveguide laser at 1.84 μm," *Opt Express*, vol. 19, no. 2, pp. 1449-1454, 2011/01/17 2011, doi: 10.1364/OE.19.001449.
[24] Y. N. Korkishko, V. A. Fedorov, T. M. Morozova, F. Caccavale, F. Gonella, and F. Segato, "Reverse proton exchange for buried waveguides in LiNbO3," *J. Opt. Soc. Am. A*, vol. 15, no. 7, pp. 1838-1842, 1998/07/01 1998, doi: 10.1364/JOSAA.15.001838.
[25] H. Uetsuhara, S. Goto, Y. Nakata, N. Vasa, T. Okada, and M. Maeda, "Fabrication of a Ti:sapphire planar waveguide by pulsed laser deposition," *Applied Physics A*, vol. 69, no. 1, pp. S719-S722, 1999/12/01 1999, doi: 10.1007/s003390051514.
[26] F. Chen and J. R. V. de Aldana, "Optical waveguides in crystalline dielectric materials produced by femtosecond- laser micromachining," (in English), *Laser Photonics Rev*, vol. 8, no. 2, pp. 251-275, Mar 2014, doi: 10.1002/lpor.201300025.
[27] R. Osellame, G. Cerullo, and R. Ramponi, *Femtosecond laser micromachining: photonic and microfluidic devices in transparent materials*. Springer, 2012.

[28] J. Burghoff, S. Nolte, and A. Tünnermann, "Origins of waveguiding in femtosecond laser-structured LiNbO3," *Applied Physics A,* vol. 89, no. 1, pp. 127-132, 2007/10/01 2007, doi: 10.1007/s00339-007-4152-0.

[29] V. Apostolopoulos *et al.*, "Femtosecond-irradiation-induced refractive-index changes and channel waveguiding in bulk Ti3+:Sapphire," *Applied Physics Letters,* vol. 85, no. 7, pp. 1122-1124, 2004, doi: 10.1063/1.1781737.

[30] T. Gorelik, M. Will, S. Nolte, A. Tuennermann, and U. Glatzel, "Transmission electron microscopy studies of femtosecond laser induced modifications in quartz," *Applied Physics A,* vol. 76, no. 3, pp. 309-311, 2003/03/01 2003, doi: 10.1007/s00339-002-1813-x.

[31] A. Ródenas *et al.*, "Refractive index change mechanisms in femtosecond laser written ceramic Nd: YAG waveguides: micro-spectroscopy experiments and beam propagation calculations," *Applied Physics B,* vol. 95, pp. 85-96, 2009.

[32] G. Fibich and A. L. Gaeta, "Critical power for self-focusing in bulk media and in hollow waveguides," *Optics letters,* vol. 25, no. 5, pp. 335-337, 2000.

[33] S. M. Eaton *et al.*, "Heat accumulation effects in femtosecond laser-written waveguides with variable repetition rate," *Opt Express,* vol. 13, no. 12, pp. 4708-4716, 2005.

[34] S. Juodkazis, H. Misawa, and I. Maksimov, "Thermal accumulation effect in three-dimensional recording by picosecond pulses," *Applied Physics Letters,* vol. 85, no. 22, pp. 5239-5241, 2004.

[35] A. Benayas *et al.*, "Ultrafast laser writing of optical waveguides in ceramic Yb: YAG: a study of thermal and non-thermal regimes," *Applied Physics A,* vol. 104, pp. 301-309, 2011.

[36] J. Burghoff, C. Grebing, S. Nolte, and A. Tünnermann, "Efficient frequency doubling in femtosecond laser-written waveguides in lithium niobate," *Applied physics letters,* vol. 89, no. 8, p. 081108, 2006.

[37] J. R. MacDonald, R. Thomson, S. Beecher, N. Psaila, H. Bookey, and A. Kar, "Ultrafast laser inscription of near-infrared waveguides in polycrystalline ZnSe," *Optics letters,* vol. 35, no. 23, pp. 4036-4038, 2010.

[38] A. Rodenas and A. K. Kar, "High-contrast step-index waveguides in borate nonlinear laser crystals by 3D laser writing," *Opt Express,* vol. 19, no. 18, pp. 17820-17833, 2011.

[39] I. Aharonovich, A. D. Greentree, and S. Prawer, "Diamond photonics," (in English), *Nat Photonics,* vol. 5, no. 7, pp. 397-405, Jul 2011, doi: 10.1038/Nphoton.2011.54.

[40] A. Sabella, D. J. Spence, and R. P. Mildren, "Pump–probe measurements of the Raman gain coefficient in crystals using multi-longitudinal-mode beams," *IEEE Journal of Quantum Electronics,* vol. 51, no. 12, pp. 1-8, 2015.

[41] A. Sabella, J. A. Piper, and R. P. Mildren, "1240 nm diamond Raman laser operating near the quantum limit," (in English), *Optics Letters,* vol. 35, no. 23, pp. 3874-3876, Dec 1 2010, doi: Doi 10.1364/Ol.35.003874.

[42] A. Sabella, J. A. Piper, and R. P. Mildren, "Diamond Raman laser with continuously tunable output from 3.38 to 3.80 mu m," (in English), *Optics Letters,* vol. 39, no. 13, pp. 4037-4040, Jul 1 2014, doi: 10.1364/Ol.39.004037.

[43] B. J. M. Hausmann, I. Bulu, V. Venkataraman, P. Deotare, and M. Loncar, "Diamond nonlinear photonics," (in English), *Nat Photonics,* vol. 8, no. 5, pp. 369-374, May 2014, doi: 10.1038/nphoton.2014.72.

[44] E. Ampem-Lassen *et al.*, "Nano-manipulation of diamond-based single photon sources," *Opt Express,* vol. 17, no. 14, pp. 11287-11293, 2009.
[45] B. Sotillo *et al.*, "Diamond photonics platform enabled by femtosecond laser writing," *Sci Rep,* vol. 6, p. 35566, Oct 17 2016, doi: 10.1038/srep35566.
[46] A. Courvoisier, M. J. Booth, and P. S. Salter, "Inscription of 3D waveguides in diamond using an ultrafast laser," (in English), *Applied Physics Letters,* vol. 109, no. 3, Jul 18 2016, doi: Artn 031109
10.1063/1.4959267.
[47] B. Sotillo *et al.*, "Visible to Infrared Diamond Photonics Enabled by Focused Femtosecond Laser Pulses," *Micromachines,* vol. 8, no. 2, 2017, doi: 10.3390/mi8020060.
[48] J. P. Hadden *et al.*, "Integrated waveguides and deterministically positioned nitrogen vacancy centers in diamond created by femtosecond laser writing," *Opt Lett,* vol. 43, no. 15, pp. 3586-3589, Aug 1 2018, doi: 10.1364/OL.43.003586.
[49] B. Sotillo *et al.*, "Polarized micro-Raman studies of femtosecond laser written stress-induced optical waveguides in diamond," *Applied Physics Letters,* vol. 112, no. 3, 2018, doi: 10.1063/1.5017108.
[50] V. Bharadwaj, Y. Wang, T. T. Fernandez, R. Ramponi, S. M. Eaton, and G. Galzerano, "Femtosecond laser written diamond waveguides: A step towards integrated photonics in the far infrared," *Optical Materials,* vol. 85, pp. 183-185, 2018, doi: 10.1016/j.optmat.2018.08.062.
[51] V. Bharadwaj *et al.*, "Femtosecond laser written photonic and microfluidic circuits in diamond," *Journal of Physics: Photonics,* vol. 1, no. 2, 2019, doi: 10.1088/2515-7647/ab0c4e.
[52] H. Hanafi, S. Kroesen, G. Lewes-Malandrakis, C. Nebel, W. H. P. Pernice, and C. Denz, "Polycrystalline diamond photonic waveguides realized by femtosecond laser lithography," *Optical Materials Express,* vol. 9, no. 7, 2019, doi: 10.1364/ome.9.003109.
[53] S. M. Eaton *et al.*, "Quantum Micro-Nano Devices Fabricated in Diamond by Femtosecond Laser and Ion Irradiation," (in English), *Adv Quantum Technol,* vol. 2, no. 5-6, Jun 2019, doi: UNSP 1900006
10.1002/qute.201900006.
[54] V. Bharadwaj *et al.*, "Femtosecond laser written photonic and microfluidic circuits in diamond," (in English), *J Phys-Photonics,* vol. 1, no. 2, Apr 1 2019, doi: ARTN 022001
10.1088/2515-7647/ab0c4e.
[55] M. Hoese *et al.*, "Integrated Magnetometry Platform with Stackable Waveguide-Assisted Detection Channels for Sensing Arrays," *Physical Review Applied,* vol. 15, no. 5, 2021, doi: 10.1103/PhysRevApplied.15.054059.
[56] K. K. Ashikkalieva *et al.*, "Internal structure and conductivity of laser-induced graphitized wires inside diamond," (in English), *Diam Relat Mater,* vol. 128, Oct 2022, doi: ARTN 109243
10.1016/j.diamond.2022.109243.
[57] T. V. Kononenko *et al.*, "Microstructuring of diamond bulk by IR femtosecond laser pulses," (in English), *Appl Phys a-Mater,* vol. 90, no. 4, pp. 645-651, Mar 2008, doi: 10.1007/s00339-007-4350-9.
[58] E. Vanoort and M. Glasbeek, "Electric-Field-Induced Modulation of Spin Echoes of N-V Centers in Diamond," (in English), *Chem Phys Lett,* vol. 168, no. 6, pp. 529-532, May 18 1990, doi: Doi 10.1016/0009-2614(90)85665-Y.

[59] J. Lapointe, M. Gagne, M. J. Li, and R. Kashyap, "Making smart phones smarter with photonics," (in English), *Opt Express*, vol. 22, no. 13, pp. 15473-15483, Jun 30 2014, doi: 10.1364/Oe.22.015473.

[60] A. Sennaroglu, *Photonics and laser engineering : principles, devices, and applications*. New York
London: McGraw-Hill Professional
McGraw-Hill distributor (in English), 2010, pp. xxxv, 665 p. : ill.

[61] E. Kifle *et al.*, "Femtosecond-laser-written hexagonal cladding waveguide in Tm: KLu(WO4)(2): mu-Raman study and laser operation," (in English), *Optical Materials Express*, vol. 7, no. 12, pp. 4258-4268, Dec 1 2017, doi: 10.1364/Ome.7.004258.

[62] D. Marcuse, "Loss analysis of single-mode fiber splices," *Bell system technical journal*, vol. 56, no. 5, pp. 703-718, 1977.

Appendix A: Laser Beam Spot Size Measurement After Each Fabricated Waveguide

To measure the spot size of the laser beam exiting the output facet of each fabricated waveguide, the knife edge method was applied. A knife edge was mounted onto a 3D translational stage with a resolution of 10 µm, and the transverse positions of the knife edge giving 84% and 16% power transmission were measured. The spot size of each beam, which corresponds to the distance between these two positions, was measured along the propagation direction. Measurements were started from 5 mm away the output facet of the sample and continued with intervals of 5 mm until 5 measurements were taken from each waveguide. Afterwards, the spot size measurements of each waveguide were plotted as a function of the distance between the measurement point and the waveguide exit (output facet of the sample) as shown in the figures below. Therefore, the slope of the linear fit of each dataset was determined, which corresponds to the tangent of the divergence angle ($\tan\theta$). Since the divergence angles in this study are rather low, small angle approximation can be used and $\tan\theta \sim \sin\theta$ can be assumed. Finally, using the $\sin\theta$ values obtained, the Δn values in Fig. 2.4(f) were determined.

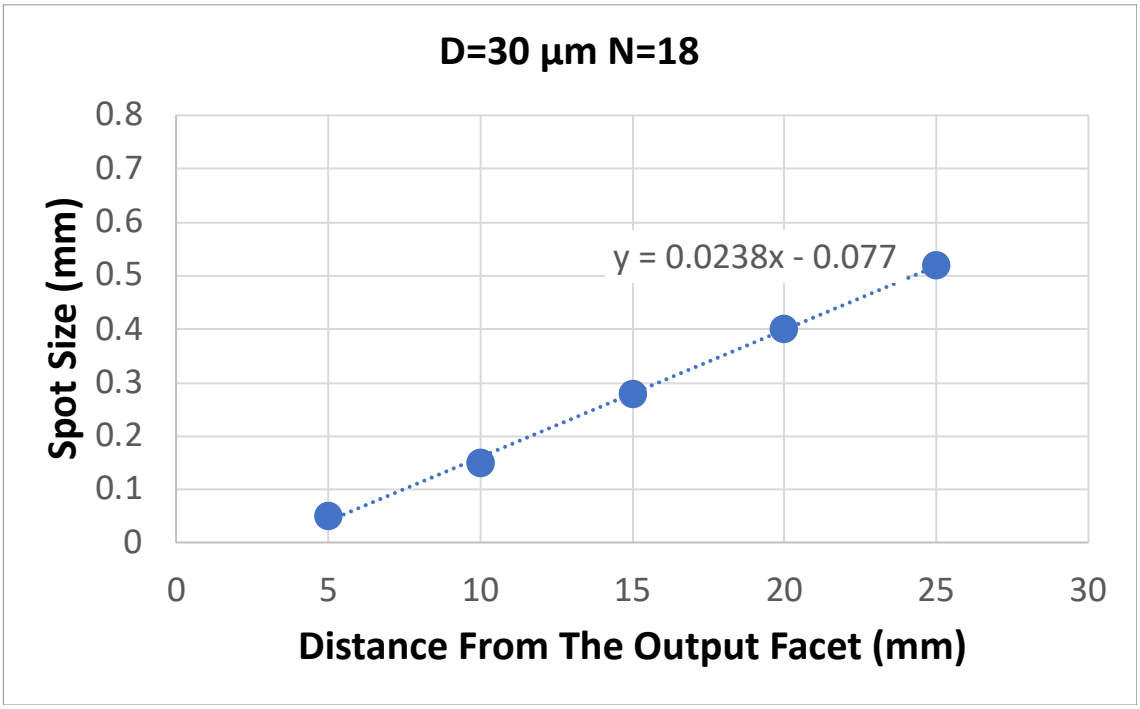

Fig.A 1: Spot size measurement of the waveguide having D=30 µm and N=18 as a function of distance.

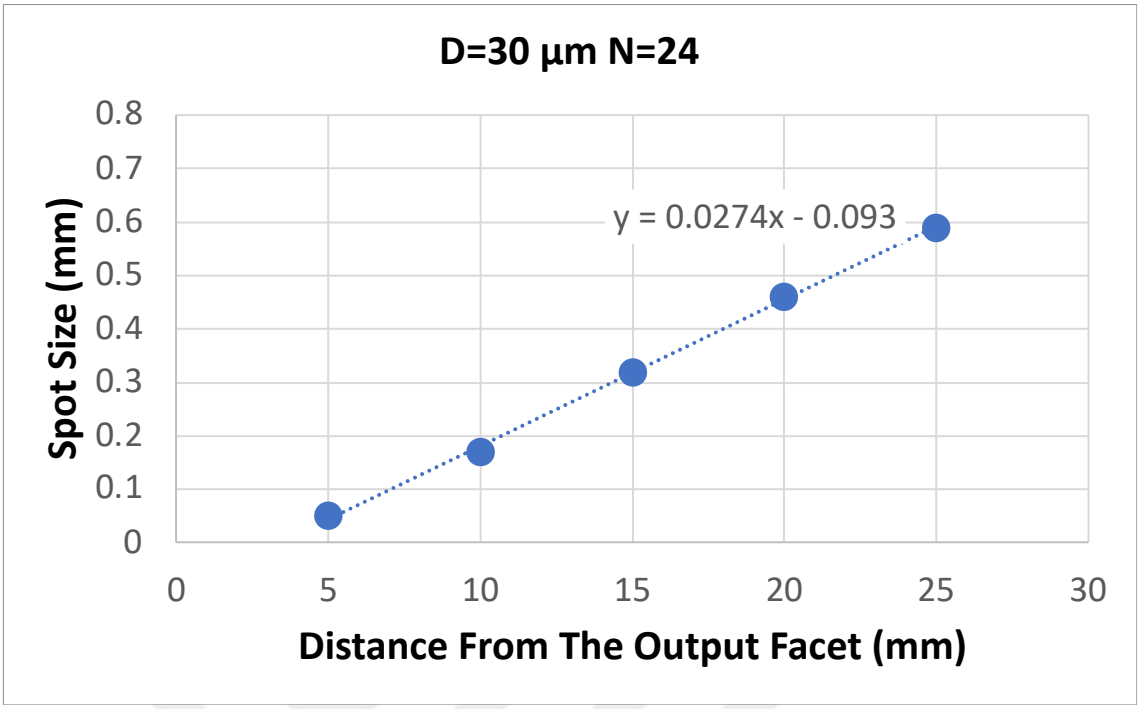

Fig.A 2: Spot size measurement of the waveguide having D=30 µm and N=24 as a function of distance.

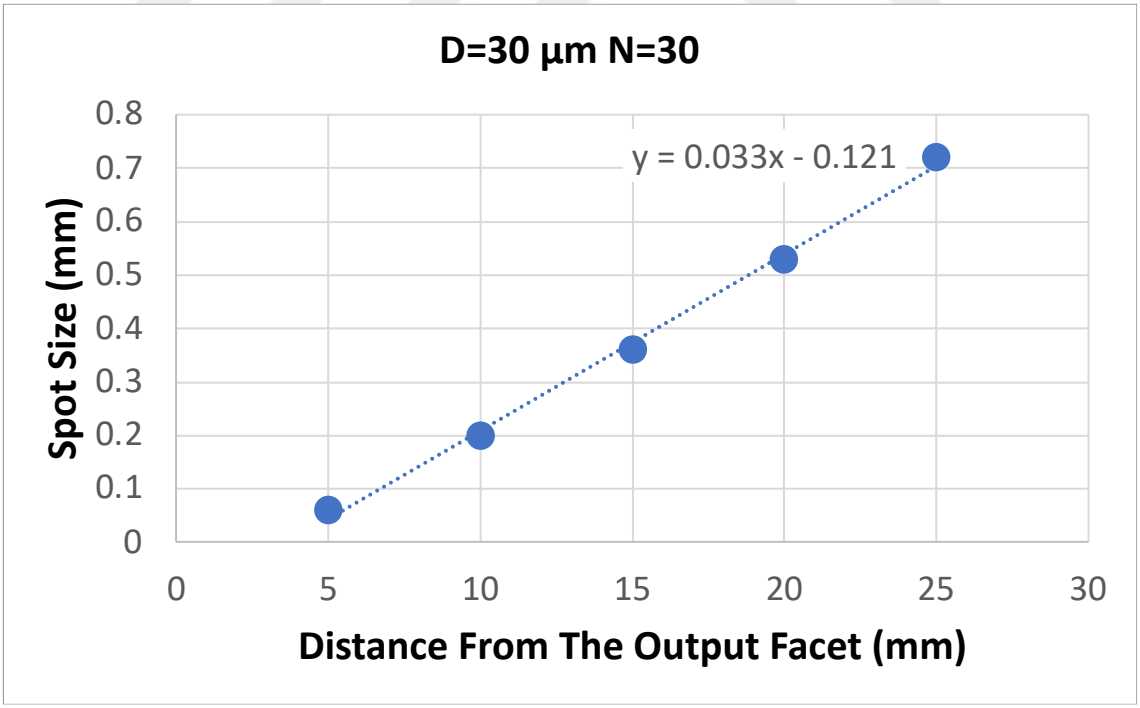

Fig.A 3: Spot size measurement of the waveguide having D=30 µm and N=30 as a function of distance.

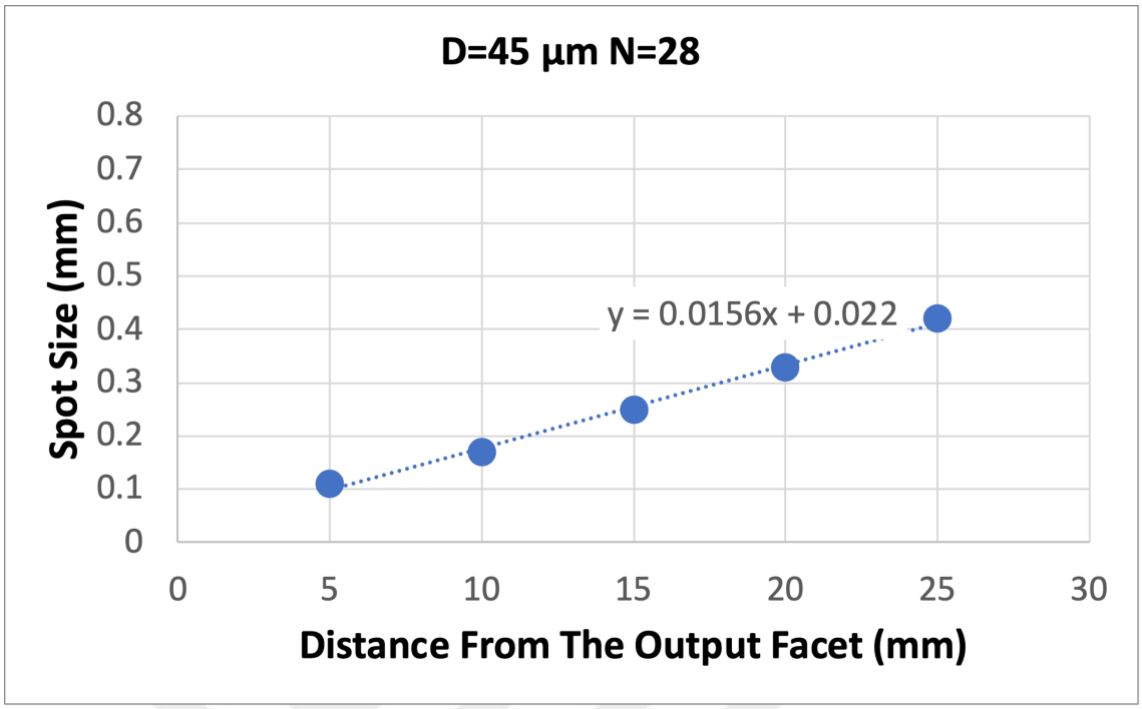

Fig.A 4: Spot size measurement of the waveguide having D=45 µm and N=28 as a function of distance.

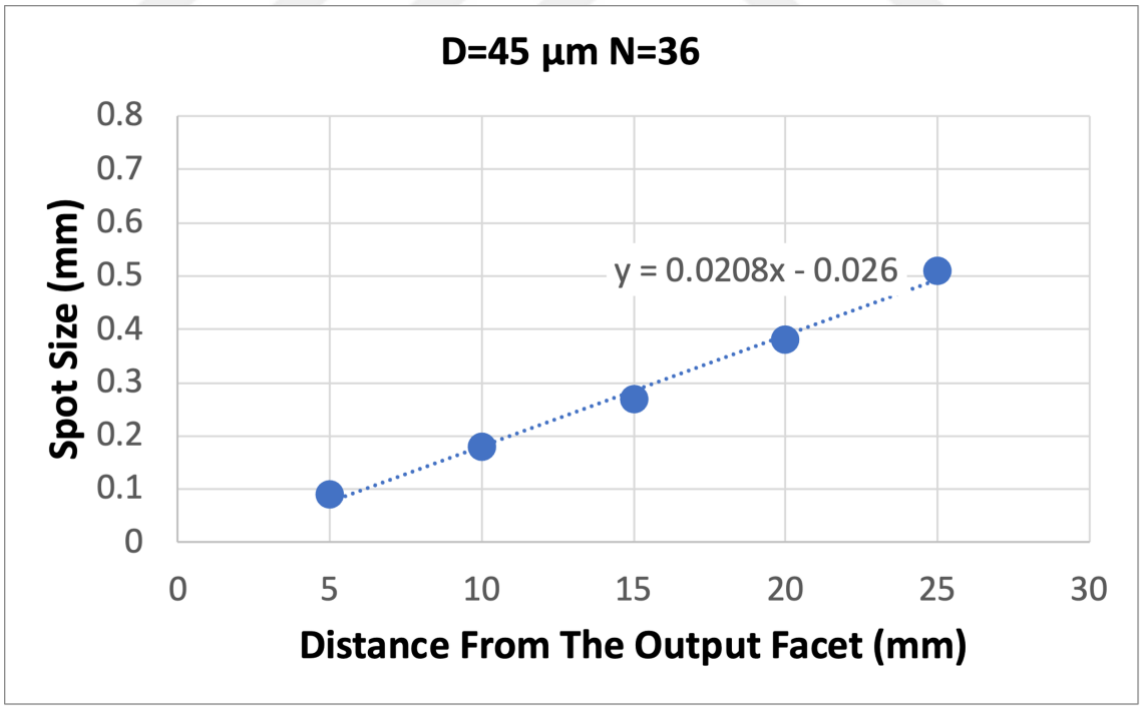

Fig.A 5: Spot size measurement of the waveguide having D=45 µm and N=36 as a function of distance.

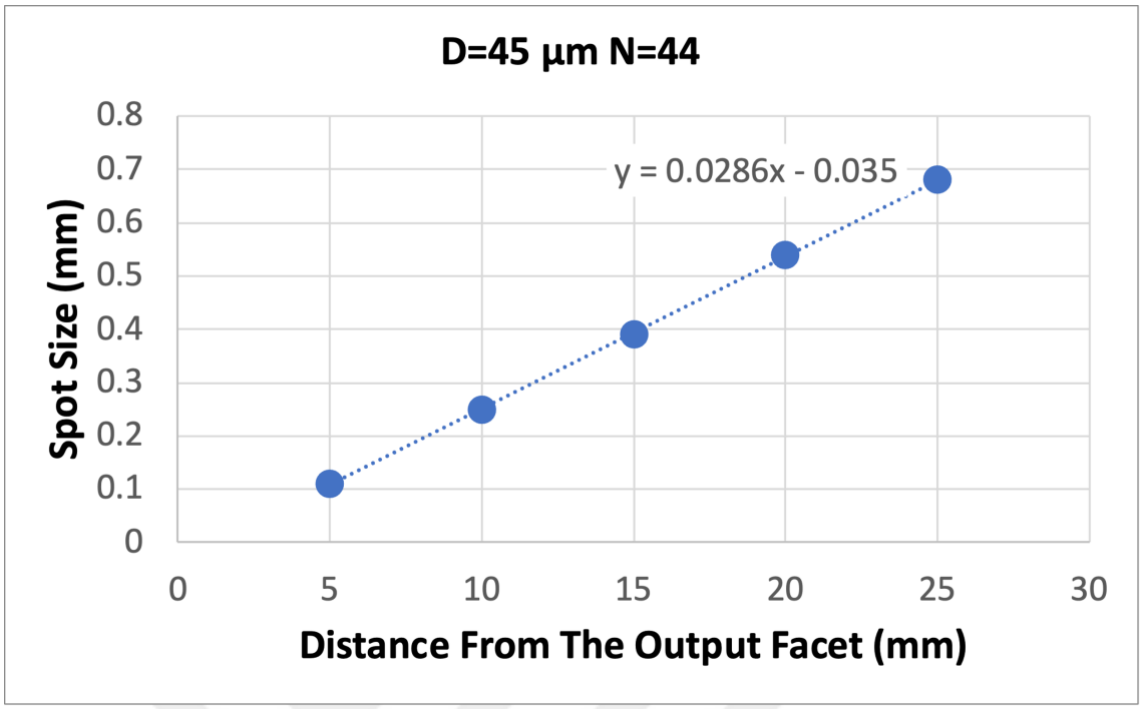

Fig.A 6: Spot size measurement of the waveguide having D=45 µm and N=44 as a function of distance.

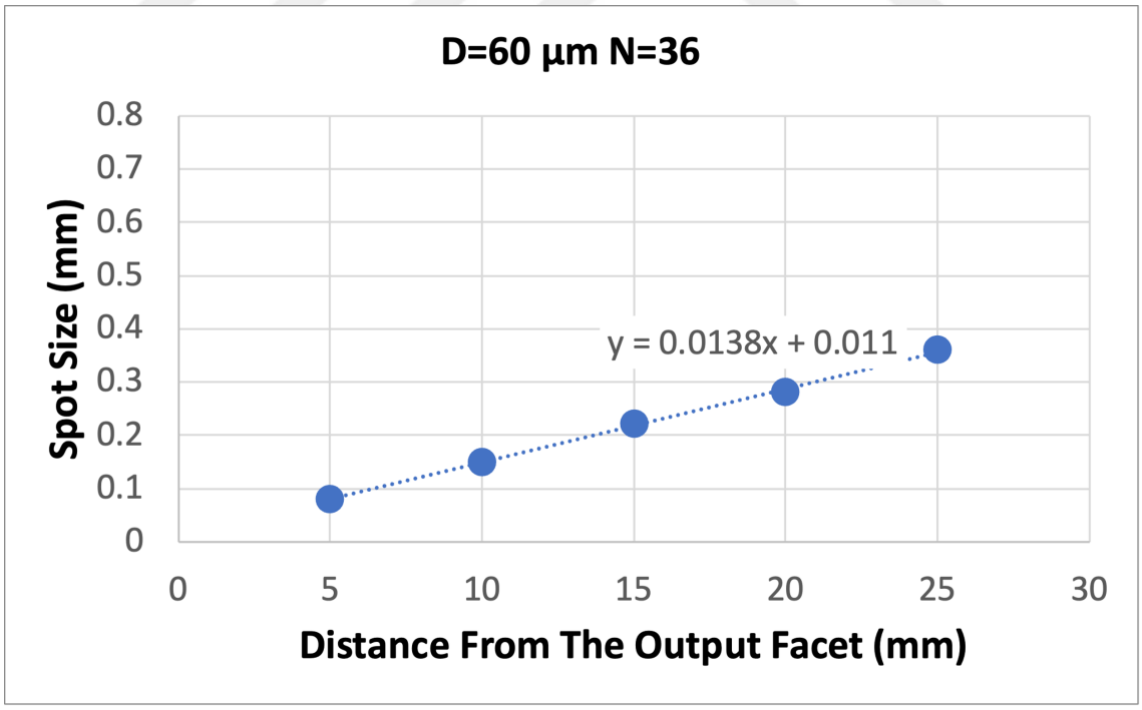

Fig.A 7: Spot size measurement of the waveguide having D=60 µm and N=36 as a function of distance.

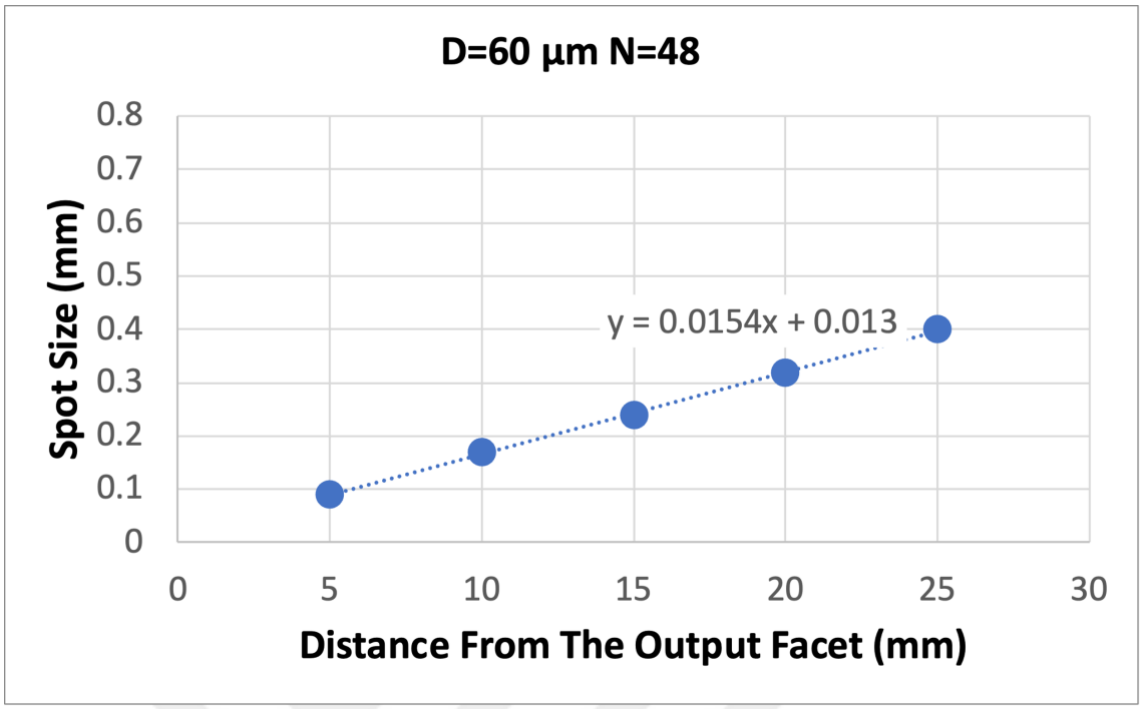

Fig.A 8: Spot size measurement of the waveguide having D=60 µm and N=48 as a function of distance.

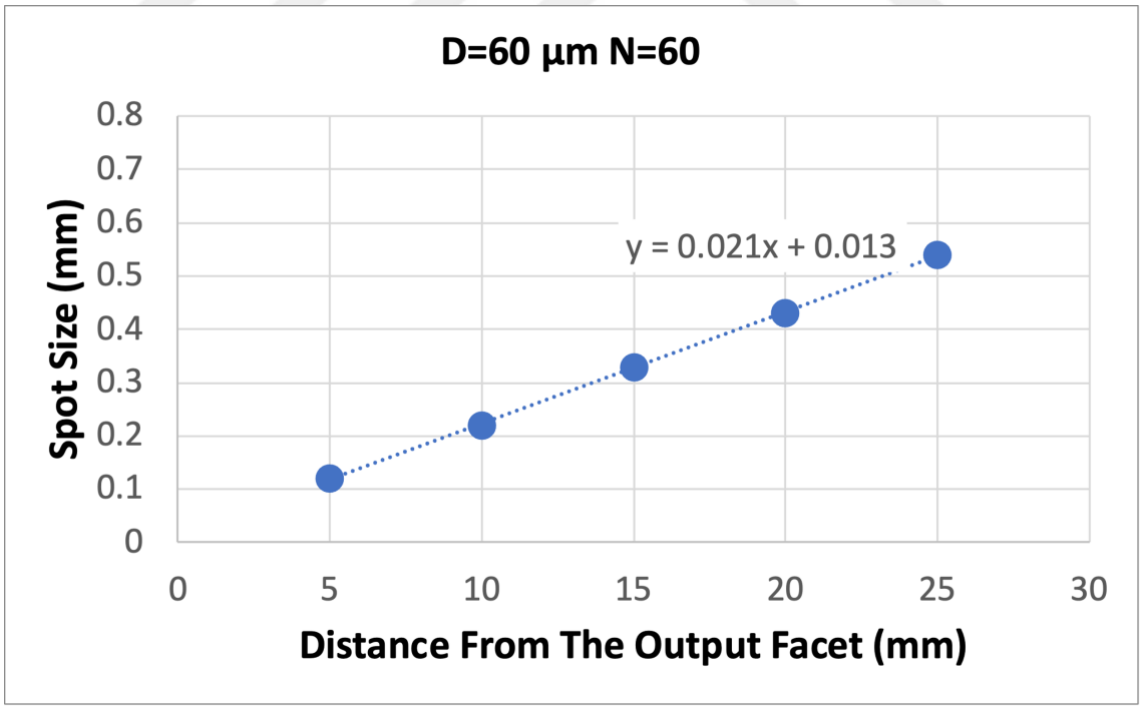

Fig.A 9: Spot size measurement of the waveguide having D=60 µm and N=60 as a function of distance.